

**An Investigation of Neutrino-Driven Convection
and the Core Collapse Supernova Mechanism
Using Multigroup Neutrino Transport**

A. Mezzacappa^{1,2}, A. C. Calder^{1,3}, S. W. Bruenn⁴, J. M. Blondin⁵,
M. W. Guidry^{1,2}, M. R. Strayer^{1,2}, and A. S. Umar³

Accepted for publication in *The Astrophysical Journal*

¹Theoretical and Computational Physics Group, Oak Ridge National Laboratory, Oak Ridge,
TN 37831-6373

²Department of Physics and Astronomy, University of Tennessee, Knoxville, TN 37996-1200

³Department of Physics and Astronomy, Vanderbilt University, Nashville, TN 37235

⁴Department of Physics, Florida Atlantic University, Boca Raton, FL 33431-0991

⁵Department of Physics, North Carolina State University, Raleigh, NC 27695-8202

Abstract

We investigate neutrino-driven convection in core collapse supernovae and its ramifications for the explosion mechanism. We begin with an “optimistic” postbounce model in two important respects: (1) we begin with a $15 M_{\odot}$ precollapse model, which is representative of the class of stars with compact iron cores; (2) we implement Newtonian gravity. Our precollapse model is evolved through core collapse and bounce in one dimension using multigroup (neutrino-energy-dependent) flux-limited diffusion (MGFLD) neutrino transport and Newtonian Lagrangian hydrodynamics, providing realistic initial conditions for the postbounce convection and evolution.

Our two-dimensional simulation began at 12 ms after bounce and proceeded for 500 ms. We couple two-dimensional (PPM) hydrodynamics to precalculated one-dimensional MGFLD neutrino transport. (The neutrino distributions used for matter heating and deleptonization in our 2D run are obtained from an accompanying 1D simulation. The accuracy of this approximation is assessed.) For the moment we sacrifice dimensionality for realism in other aspects of our neutrino transport. MGFLD is an implementation of neutrino transport that simultaneously (a) is multigroup and (b) simulates with sufficient realism the transport of neutrinos in opaque, semitransparent, and transparent regions. Both are crucial to the accurate determination of postshock neutrino heating, which sensitively depends on the luminosities, spectra, and flux factors of the electron neutrinos and antineutrinos emerging from their respective neutrinospheres.

By 137 ms after bounce, we see neutrino-driven convection rapidly developing beneath the shock. By 212 ms after bounce, this convection becomes large-scale, characterized by higher-entropy, expanding upflows and denser, lower-entropy, finger-like downflows. The upflows reach the shock and distort it from sphericity. The radial convection velocities at this time become supersonic just below the shock, reaching magnitudes in excess of 10^9 cm/sec. Eventually, however, the shock recedes to smaller radii, and at ~ 500 ms after bounce there is no evidence in our simulation of an explosion or of a developing explosion.

Our angle-averaged density, entropy, electron fraction, and radial velocity profiles in our

two-dimensional model agree well with their counterparts in our accompanying one-dimensional MGFLD run above and below the neutrino-driven convection region. In the convective region, the one-dimensional and angle-averaged profiles differ somewhat because (1) convection tends to flatten the density, entropy, and electron fraction profiles, and (2) the shock radius is boosted somewhat by convection. However, the differences are not significant, indicating that, while vigorous, neutrino-driven convection in our model does not have a significant impact on the overall shock dynamics.

The differences between our results and those of other groups are considered. These most likely result from differences in (1) numerical hydrodynamics methods, (2) initial postbounce models, and most important, (3) neutrino transport approximations. We have compared our neutrino luminosities, RMS energies, and inverse flux factors with those from the exploding models of other groups. Above all, we find that the neutrino RMS energies computed by our multigroup (MGFLD) transport are significantly lower than the values obtained by Burrows *et al.*, who specified their neutrino spectra by tying the neutrino temperature to the matter temperature at the neutrinosphere and by choosing the neutrino degeneracy parameter arbitrarily, and by Herant *et al.* in their transport scheme, which (1) is gray and (2) patches together optically thick and thin regions. The most dramatic difference between our results and those of Janka and Müller is exhibited by the difference in the net cooling rate below the gain radii: Our rate is 2–3 times greater during the critical 50–100 milliseconds after bounce.

We have computed the mass and internal energy in the gain region as a function of time. Up to ~ 150 ms after bounce, we find that both increase as a result of the increasing gain region volume, as the gain and shock radii diverge. However, at all subsequent times we find that the mass and internal energy in the gain region decrease with time in accordance with the density falloff in the preshock region and with the flow of matter into the gain region at the shock and out of the gain region at the gain radius. Therefore, we see no evidence in the simulations presented here that neutrino-driven convection leads to mass and energy accumulation in the gain region.

We have compared our 1- and 2D densities, temperatures, and electron fractions in the region

below the electron neutrino and antineutrino gain radii, above which the neutrino luminosities are essentially constant (i.e., the neutrino sources are entirely enclosed), in an effort to assess how spherically symmetric our neutrino sources remain during our 2D evolution, and therefore, to assess our use of precalculated 1D MGFLD neutrino distributions in calculating the matter heating and deleptonization. We find no differences below the neutrinosphere radii, and between the neutrinosphere and gain radii, no differences with obvious ramifications for the supernova outcome. We note that the interplay between neutrino transport and convection below the neutrinospheres is a delicate matter, and is discussed at greater length in another paper (Mezzacappa *et al.* 1997a). However, the results presented therein do support our use of precalculated 1D MGFLD in the present context.

Failure in our “optimistic” $15 M_{\odot}$ Newtonian model leads us to conclude that it is unlikely, at least in our approximation, that neutrino-driven convection will lead to explosions for more massive stars with fatter iron cores or in cases in which general relativity is included.

Subject headings: (stars:) supernovae: general – convection

1. Introduction

1.1. Convection and the Supernova Mechanism

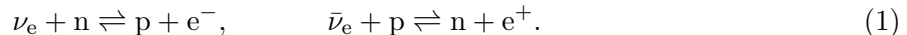
Much of the current research on the core collapse supernova mechanism is focused on the role of convection. This is motivated in part by a number of observations of SN 1987A, which indicate that extensive mixing occurred throughout much of the ejected material, which, by inference, points to fluid instabilities arising during the explosion itself. The early (July, 1987) detection of continuum X-rays and γ -rays (Dotani *et al.* 1987; Sunyaev *et al.* 1987) and of the 847 and 1238 keV ^{56}Co γ -ray lines (August, 1987) (Matz, Share, & Chupp 1988; Matz *et al.* 1988), confirmed shortly thereafter by others (Cook *et al.* 1988; Gehrels, Leventhal, & MacCallum 1988; Mahoney *et al.* 1988; Sandie *et al.* 1988; Wilson *et al.* 1988; Teegarden *et al.* 1989), suggests that mixing of the ^{56}Co in the ejecta must have occurred. ^{56}Co arises from ^{56}Ni , which is created in the deep silicon layer. Without the breaking of spherical symmetry, ^{56}Co and other radioactive elements would remain buried under the massive stellar envelope for about a year, until the latter became transparent by expansion (Gehrels, MacCallum, & Leventhal 1987; McCray, Shull, & Sutherland 1988; Pinto & Woosley 1988; Xu *et al.* 1988). Even more direct evidence of significant mixing is the very high Fe velocities ($\gtrsim 3000 \text{ km s}^{-1}$) inferred from infrared observations of ^{56}Fe II lines (Erikson *et al.* 1988; Rank *et al.* 1988; Hass *et al.* 1990; Spyromilio, Meikle, & Allen 1990), the very large ^{56}Co velocities inferred from the 847 keV line profile by the GRIS experiment (Tueller *et al.* 1990), and hydrogen velocities as low as 800 km s^{-1} (Höflich 1988). These observables are evidence that some of the ^{56}Ni (the progenitor of ^{56}Co and ^{56}Fe) was mixed out to the hydrogen envelope. Because this degree of mixing is not reproduced by simulations in which the mixing arises only from Rayleigh–Taylor instabilities in the expanding envelope (Arnett, Fryxell, & Müller 1989; Den, Yoshida, & Yamada 1990; Hachisu *et al.* 1990; Yamada, Nakamura, & Oohara 1990; Fryxell, Arnett, & Müller 1991; Müller, Fryxell, & Arnett 1991; Herant & Benz 1991, 1992), it must be presumed that these instabilities were preceded by a prior round of instabilities, most likely occurring in the explosion itself (Herant & Benz 1992).

In addition to the observational evidence of extensive mixing due to fluid instabilities, there are compelling theoretical reasons to consider convection. The first and obvious reason is that there are several unstable regions that develop in the postcollapse core, both below and above the neutrinosphere (Epstein 1979; Arnett 1986, 1987; Bethe, Brown, & Cooperstein 1987; Burrows 1987; Bethe 1990). The second is the failure to explode of supernova simulations that do not incorporate fluid instabilities (Bruenn 1993; Cooperstein 1993; Wilson and Mayle 1993), and the expectation that fluid instabilities, by enhancing the transport of lepton-rich matter to the neutrinosphere or augmenting the neutrino energy deposition efficiency above the neutrinosphere, will be helpful in generating explosions. These expectations derive from the nature of the explosion “power up” phase, as envisioned by the current core collapse supernova paradigm. According to this paradigm, which is referred to as the “shock reheating mechanism” or “delayed mechanism” (Wilson 1985; Bethe and Wilson 1985), the shock launched into the outer core at core bounce stalls between 100 and 200 km due to nuclear dissociation and neutrino radiation. The shock then becomes an accretion shock, and within 10’s of milliseconds, a quasi-steady-state structure is established in which infalling matter encountering the shock is dissociated into free nucleons and then heated by the transfer and deposition of energy by neutrinos radiating from the hot contracting core. As this matter continues to flow inward, neutrino and compressional heating increase its temperature until the cooling rate, which goes as the sixth power of the temperature, exceeds the heating rate. The inflowing matter thereafter cools and eventually accretes onto the core. The radius at which the heating and cooling rates are equal is referred to as the “gain radius.” If the neutrino heating is sufficiently rapid in the region between the shock and the gain radius, the increased thermal pressure behind the shock will allow it to overcome the accretion ram pressure and propagate out through the envelope, thus producing a supernova.

1.2. Fluid Instabilities: Preliminaries

We emphasize again that spherically symmetric supernova simulations that have not incorporated fluid instabilities fail to provide the necessary heating to revive the shock. To

appreciate the potential role of fluid instabilities in reviving the shock, we begin with the fact that the energy transfer between neutrinos and matter behind the shock is mediated primarily by the charged current reactions:



It follows that the heating and cooling rates by ν_e 's are given by

$$\frac{\text{Heating}}{\text{Nucleon}} \propto L_{\nu_e} \langle \epsilon_{\nu_e}^2 \rangle \left\langle \frac{1}{\mathcal{F}_{\nu_e}} \right\rangle \quad (2)$$

$$\frac{\text{Cooling}}{\text{Nucleon}} \propto T_m^6 \quad (3)$$

with similar expressions for the $\bar{\nu}_e$'s. Here, L_{ν_e} is the ν_e luminosity; $\langle \epsilon_{\nu_e}^2 \rangle$ is the ν_e mean square energy, averaged with respect to $\epsilon_{\nu_e}^3$; $\frac{1}{\mathcal{F}_{\nu_e}} \gtrsim 1$ is the inverse flux factor, which equals $c \times U_{\nu_e}/F_{\nu_e}$, where U_{ν_e} and F_{ν_e} are the ν_e energy density and flux, respectively; and T_m is the local matter temperature. We have neglected the electron degeneracy of the matter in equation (3).

1.3. Fluid Instabilities below the Neutrinosphere

Fluid instabilities occur in several distinct regions in a postcollapse stellar core. Near and below the neutrinosphere, the dissipation of the shock due to nuclear dissociation and ν_e radiation will imprint a negative entropy gradient, and therefore destabilize this region to entropy-driven convection (Arnett 1986, 1987; Burrows 1987). While the convection will not be sustained, it can lead to a rapid initial turnover of the region. The material near and below the neutrinosphere will also be destabilized by a negative lepton gradient (Epstein 1979). This results from the lepton “trough” produced near the neutrinosphere by the combination of rapid electron capture and ν_e escape. A negative lepton gradient connects this region with the more lepton-rich material at smaller radii. Because electron capture and ν_e radiation continues near the neutrinosphere as

the protoneutron star evolves, the tendency of lepton-driven fluid motions to flatten the negative lepton gradient will be resisted, and the instability driving these fluid motions may tend to persist. Deeper in the core, the destabilizing effect of the negative lepton gradient will be counteracted by the stabilizing effect of the positive entropy gradient left over from the shock as it propagates through this region while gathering strength from the rebounding inner core. With the diffusion of both energy and leptons by neutrinos, this region can be destabilized on a diffusion timescale, if the diffusion rates for energy and leptons are different. Mayle (1995) and Wilson and Mayle (1988, 1993) have argued that the material in this region will be unstable to one of these doubly diffusive instabilities referred to as “neutron fingers.” Bruenn, Mezzacappa and Dineva (1995) and Bruenn and Dineva (1996) have disputed this claim. It is not our purpose here to delve deeper into the nature or existence of the possible modes of fluid instabilities below the neutrinosphere. Let us simply refer in the following to the fluid motions that would result from any of the above fluid instabilities as “protoneutron star convection.” In most cases, protoneutron star convection will be confined to the region below and encompassing the neutrinosphere.

The effect of protoneutron star convection on shock heating can be ascertained by referring to equation (2), where it is seen that the heating rate depends on the product of the factors L_{ν_e} , $\langle \epsilon_{\nu_e}^2 \rangle$, and $\langle \frac{1}{\mathcal{F}_{\nu_e}} \rangle$. The last of these factors, the inverse flux factor, is primarily geometrical, depending on the ratio of the neutrinosphere radius to the radial distance of the fluid element in question. It approaches unity, as this ratio becomes small, reflecting the fact that the neutrinos are radially free streaming in this limit. However, the first two factors depend on the conditions at the neutrinosphere, and can therefore be affected by protoneutron star convection. Let us suppose that the neutrinosphere lies near the bottom of a negative entropy gradient. Then entropy-driven protoneutron star convection will advect high-entropy material from deeper regions, up to the vicinity of the neutrinosphere, raising the temperature there. This will clearly increase both L_{ν_e} and $\langle \epsilon_{\nu_e}^2 \rangle$, with similar consequences for the corresponding $\bar{\nu}_e$ quantities. (This is obvious in the limit of zero electron degeneracy, where the product of these two factors is proportional to $T_{\nu_e}^6$, where T_{ν_e} is the ν_e -sphere temperature.) In addition to increasing the neutrinosphere temperature, protoneutron star convection can also increase the neutrinospheric lepton fraction. This follows

from the fact that rapid electron capture and ν_e escape at the neutrinosphere causes it to lie near a lepton fraction (Y_ℓ) minimum. Entropy- or lepton-driven protoneutron star convection will advect lepton-rich matter to the vicinity of the neutrinosphere, and thereby increase the electron degeneracy there. This will increase both L_{ν_e} and $\langle \epsilon_{\nu_e}^2 \rangle$, while decreasing $L_{\bar{\nu}_e}$ and $\langle \epsilon_{\bar{\nu}_e}^2 \rangle$. In most cases, the net effect will be to augment the heating rate of the material behind the shock.

Since the original suggestion of Epstein (1979), protoneutron star convection has been studied by a number of groups (Arnett 1986, 1987; Bethe 1990, 1993; Bruenn and Mezzacappa 1994; Bruenn, Mezzacappa, and Dineva 1995; Bruenn and Dineva 1996; Burrows 1987; Burrows and Lattimer 1988; Burrows and Fryxell 1992, 1993; Burrows, Hayes, and Fryxell 1995; Colgate, Herant, and Benz 1993; Herant, Benz, and Colgate 1992; Herant *et al.* 1994; Janka and Müller 1993, 1995, 1996; Keil, Janka, and Müller 1996; Mezzacappa *et al.* 1997a; Müller 1993; Müller and Janka 1994; Wilson and Mayle 1988, 1993;). Despite this work, the nature and extent of protoneutron star convection and its effect on shock heating is still unclear. The problem is that the coupling between neutrino transport and the fluid motions arising from instabilities in this region is strong, requiring that realistic simulations incorporate both multi-D hydrodynamics and multi-D multigroup neutrino transport. Until this has been accomplished, the picture will probably remain unclear.

1.4. Fluid Instabilities above the Neutrinosphere

As infalling material encounters the shock, it is dissociated into free neutrons and protons if the shock is within a radius ~ 200 km. (At larger radii there will be an admixture of alpha particles.) As this material continues to flow inward, it will be heated by the charged-current reactions [equation (1)], until it reaches the gain radius. Furthermore, the neutrino heating is strongest just beyond the gain radius and decreases farther out, as the neutrino flow becomes radially diluted. These two factors conspire to create a negative entropy gradient between the gain radius and the shock, which will be unstable to entropy-driven convection. Because this convection is driven by neutrino heating, it will persist as long as neutrinos heat, or until an

explosion develops. This convection, which is the subject of this paper, will be referred to as “neutrino-driven convection” or “ND convection.”

Bethe (1990) pointed out that ND convection would reduce or eliminate the density inversions found at the outer edge of the hot bubble that formed in the successful supernova simulations of Wilson and Mayle (1993). ND convection was not incorporated in these calculations, and an enormous negative density gradient developed behind the shock as it propagated out. He noted also that neutrino-driven convection would bring cooler material down to the vicinity of the gain radius where it would be more efficiently heated, because the cooling rate, as given by equation (3), would be reduced; the outward flow of hot material would bring energy to the shock, and thus help to support it.

The first 2D supernova simulation incorporating ND convection was performed by Herant, Benz, and Colgate (1992) using a smooth-particle-hydrodynamics (SPH) code. They found that, if ND convection is able to develop, it plays a crucial role in generating an efficient explosion. The convective flows in their calculations became large-scale “long-wavelength” flows, providing an efficient (separate hot and cold matter) way of conveying low-entropy matter from the shock to the gain radius and high-entropy matter back to the shock. Furthermore, the latent heat of the alpha-free-nucleon transition enables the storage and transport of large amounts of energy without large temperature increases. They noted finally that ND convection would allow accretion to continue while the shock is moving outward in radius, thereby maintaining an energy input to the shock from the neutrinos radiated by the accreting matter. Colgate, Herant, and Benz (1993) examined the accretion onto the neutron star during the explosion [the Herant, Benz, and Colgate (1992) simulations could not resolve this aspect of the problem, and they ignored the contribution to the neutrino luminosity by the accreting matter], and suggested that accretion would be unstable, leading to episodic bursts of high-energy neutrinos that would be efficiently absorbed by the overlying material. This conjecture has not yet been confirmed. In a set of more refined and self-consistent calculations, Herant *et al.* (1994) confirmed the conclusions of Herant, Benz, and Colgate (1992), and emphasized the large-scale character of ND convection and its role

in producing robust and self-regulated supernova explosions. They concluded that ND convection is a powerful “convective engine” that feeds energy into the shock until the required explosion energy has been reached. Thus, ND convection almost guarantees a successful explosion.

A simulation using entirely different numerical techniques by Miller, Wilson, and Mayle (1993) reached a very different conclusion. They used a semi-Eulerian finite-difference method (Bowers and Wilson 1991), and a combination of light-bulb and two-temperature diffusion schemes for neutrino transport, calibrated by their sophisticated 1D code. As in the Herant, Benz, and Colgate (1992) and the Herant *et al.* (1994) simulations, they found that ND convection tended to evolve to a large-scale, long-wavelength flow. However, the growth rates for their convection were much slower, *e.g.*, an e-folding time of 13 ms, versus a fully developed convection in 20–25 ms after bounce. Because their convection growth rates were slow, and because the unstable conditions for convection’s growth are not well established until ~ 0.1 second after bounce, Miller, Wilson, and Mayle (1993) found that ND convection was not particularly important in their simulations. Acknowledging that the limitations of their 2D model favored explosions, they concluded that more realistic 2D simulations would show that the effects of ND convection are unlikely to revive a stalled shock.

2D supernova simulations using hydrodynamics codes based on the piecewise-parabolic-method (PPM) of Colella and Woodward (1994) and incorporating ND convection were performed by Burrows, Hayes, and Fryxell (1995), and by Janka and Müller (1995, 1996). In contrast to the results of Herant *et al.* and Miller *et al.*, the PPM calculations found ND convection to be more turbulent, although a large-scale flow was exhibited. The flows consisted of high-entropy rising bubbles and balloons, distorted into mushrooms by Kelvin-Helmholtz instabilities, and low-entropy descending narrow flux tubes; and the mode numbers ranged from 2 to 10. Burrows, Hayes, and Fryxell (1995) implemented radial transport along their angular rays in a gray diffusion approximation for optical depths $\geq 1/2$, with a neutrino-matter coupling for optical depths $\leq 1/2$ that assumes particular electron neutrino and antineutrino energy spectra. Unlike the Herant *et al.* simulations, they found that neither mass nor energy accumulate in the convection region.

They were unable to verify the basic “convective engine” paradigm of Herant *et al.* and found, instead, that if an explosion ensues, it is because of the decline in the accretion ram, rather than an increase in the shock energy [see also Burrows and Goshy (1993)]. They found that ND convection allows higher entropies to develop in the convective region than in 1D simulations because of the longer time a given fluid element spends in the gain region (1 or 2 cycle times before passing inward through the gain radius). This combined with the dynamic pressure of the buoyant plumes causes the stalled shock radius to equilibrate at a larger value and therefore at a lower gravitational potential. The corresponding reduction in the accretion ram makes it easier for 2D supernova models to explode, but does not guarantee an explosion. Reducing the magnitudes of the neutrino-matter coupling terms by assuming a different neutrino spectrum led to failures.

Janka and Müller (1995, 1996) performed a very useful parameter study of 1D and 2D supernova simulations by varying a light-bulb neutrino source. Like Burrows *et al.*, and unlike Herant *et al.*, they did not find an accumulation of energy in the ND convection region until the typical value of 10^{51} erg was reached. However, unlike the Burrows *et al.* simulations, their simulations did not exhibit the vigorous boiling that immediately preceded an explosion. They also found that accretion onto the protoneutron star ceased when an explosion got underway; therefore, the explosion was not continuously fed by accretion luminosity. They did find that ND convection leads to a higher net efficiency of neutrino energy deposition and an efficient mechanism of transporting energy to the shock. Their overall conclusions were that ND convection is important for generating explosions only in a rather narrow window ($\Delta L/L \sim 20\%$) of neutrino luminosities. Below this window, neither 1D nor 2D simulations would explode; above this window, both would explode.

1.5. This Work

It is apparent from the above discussion that there is considerable disagreement regarding the role of ND convection in the supernova mechanism. All of the above simulations were pioneering in the sense that multi-D hydrodynamics was used. However, computer limitations necessitated

that rather severe approximations be made in the neutrino transport and the coupling of neutrinos to matter. We feel that much of the disparity in the above results can be traced to differences in the treatment of neutrinos. In fact, we will show in this paper that the supernova simulations incorporating ND convection that give rise to explosions assume a hard neutrino spectrum (thus favoring explosions) when compared with multigroup calculations.

The purpose of this paper is to eliminate some of the uncertainties associated with neutrino transport approximations by “coupling” (the meaning of this term will be made clear below) a sophisticated multigroup flux-limited diffusion (MGFLD) neutrino transport code with the numerically nondiffusive high-order PPM hydrodynamics code, EVH-1, to examine the role of ND convection in the supernova mechanism. The importance of using multigroup neutrino transport is that the neutrino energy spectrum is part of the solution and need not be assumed. The importance of using flux-limited diffusion is that the transport of neutrinos from optically thick to optically thin regions is computed seamlessly and with sufficient realism.

Our procedure, described in more detail in Mezzacappa *et al.* (1997a), is to perform a 1D (Lagrangian) simulation of core collapse and the postbounce evolution to (1) generate running (*i.e.*, time-dependent) inner and outer boundary conditions for all of the relevant variables at our fixed inner and outer Eulerian boundaries, and (2) generate tables of the zeroth angular moments of the neutrino distributions as a function of time, radius, and neutrino energy. The 2D simulation is then carried out using the inner and outer boundary conditions generated by our 1D simulation, and the neutrino moment tables are used to compute the local energy and lepton exchange between the matter and the neutrinos.

Because ND convection occurs between the gain radius and the shock, the convecting material has small neutrino optical depths for all of the relevant neutrino energies. Thus, we expect the feedback between the hydrodynamics and the neutrino transport in this region to be minimal. If this were the entire story, coupling 1D MGFLD to 2D hydrodynamics would be an excellent approximation. However, the neutrino radiation field in the gain region is largely determined by the neutrino transport below it, particularly above and below the neutrinospheres. Therefore, to

fully assess the accuracy of 1D transport, we must consider the feedback on the radiation field that results from (1) asymmetric accretion through the gain radius from the neutrino-driven convection region and (2) nonspherically symmetric structure below the neutrinospheres that may result, for example, from protoneutron star convection [see Wilson and Mayle (1993), Herant *et al.* (1994), Burrows *et al.* (1995), Keil *et al.* (1996), and Mezzacappa *et al.* (1997a)]. We consider the first effect here. The second effect has been considered at length in Mezzacappa *et al.* (1997a), and the key results relevant to the claims made in this paper are mentioned again here (in Section 4).

In Section 2, we briefly describe our initial models, codes, and methodology. Our results are then presented in Section 3. Section 4 is devoted to an assessment of our 1D MGFLD neutrino transport approximation, and in Section 5 we summarize our results, compare them with other groups, and state our conclusions.

2. Initial Models, Codes, and Methodology

We begin with the $15 M_{\odot}$ precollapse model S15s7b (Woosley and Weaver 1995, Weaver and Woosley 1997). The initial model was evolved through core collapse and bounce using MGFLD neutrino transport and Lagrangian hydrodynamics, providing realistic initial conditions for the postbounce convection and evolution. The one-dimensional data at 12 ms after bounce (211 ms after the initiation of core collapse) were mapped onto our two-dimensional Eulerian grid. The inner and outer boundaries of our grid were chosen to be at radii of 20 km and 1000 km, respectively. 128 nonuniform radial spatial zones were used, and 128 uniform angular zones spanning a range of 180 degrees were used for θ (together with reflecting boundary conditions).

Because the finite differencing in our PPM scheme is nearly noise free, and because we cannot rely on machine roundoff to seed convection in a time that is short compared with the hydrodynamics time scales in our runs, we seeded convection everywhere on the grid by applying random velocity perturbations to the radial and angular velocities, between $\pm 5\%$ of the local sound speed. Our seeding included the initial Ledoux unstable regions below and around the neutrinospheres immediately following core bounce.

Time-dependent inner and outer boundary data for the enclosed mass, density, temperature, electron fraction, pressure, specific internal energy, and velocity were supplied by our accompanying one-dimensional MGFLD run, which was continued for this purpose for 700 ms after bounce. The inner and outer boundaries were chosen to be at 20 km (deep within the core) and at 1000 km (well outside the shock), respectively, which are regions in which the flow is spherically symmetric.

It is also important to note here that for the matter heating and deleptonization in our 2D run, we use tables of precalculated neutrino distributions, $\psi_{\nu_e, \bar{\nu}_e}^0(r, t; E_{\nu})$, obtained from our accompanying 1D run that implements MGFLD and Lagrangian hydrodynamics. Both our 1- and 2D simulations are Newtonian. The accuracy of using precalculated 1D neutrino distributions in our 2D models is discussed in Section 4.

Details of the codes used in our simulations, and more detail on our methodology, can be

found in Mezzacappa *et al.* (1997a).

3. Results

Figure 1 shows the velocity, density, entropy, and electron fraction profiles at the start of our run, 12 ms after bounce.

In Figures 2a–d we plot the results of one-dimensional simulations using our MGFLD code and our PPM hydrodynamics code. (The PPM code has been generalized for realistic equations of state and for neutrino heating and cooling and deleptonization). We compare density, entropy, electron fraction, and velocity at two different times during the course of a 500 ms run. The figures illustrate that the agreement is excellent, with the primary differences resulting from our PPM code’s ability to better resolve the shock. This gives us confidence that (1) the neutrino heating and cooling and deleptonization are simulated well by our PPM code, and (2) that differences between two-dimensional and one-dimensional simulations of the shock dynamics will result from convection’s presence in the former case, not from numerical sources.

Figure 3a shows the two-dimensional entropy profiles at three select times during our 500 ms run. At 137 ms after bounce, neutrino-driven convection is rapidly developing below the shock, having entered the nonlinear regime. There is evidence of expanding higher-entropy rising flows, and denser lower-entropy infalling matter. Roughly 7 rising plumes can be counted at this time. The convection has not yet reached the shock. By 212 ms after bounce, neutrino-driven convection is fully developed. A clear contrast is evident between the higher-entropy upflows and the lower-entropy downflows. At this time, the rising plumes have reached the shock and distorted it, and the convection is semiturbulent, although only 4 (versus 7) plumes in a range of 180 degrees can be counted now. Although more turbulent, our flow patterns are not in complete disagreement with the flows obtained by another group using SPH (Herant *et al.* 1994); the latter obtain a more orderly low-mode convection. However, differences between the SPH and PPM simulations are significant and most likely have important dynamical consequences. The low-mode convection obtained by Herant *et al.* led them to develop their “thermodynamic engine” interpretation of the supernova mechanism, although this “engine” apparently did not work in the Miller *et al.*(1993) simulations, in which low-mode convection was also exhibited. Such an interpretation is even less

possible in the PPM simulations, where high- and low-entropy flows are not as well separated. We also mention here that our flow patterns are in qualitative agreement with those obtained by other groups that implement PPM hydrodynamics (Burrows *et al.* 1995, Janka and Müller 1996). Finally, at 512 ms after bounce, Figure 3a illustrates that our shock has receded to smaller radii, and that the convection beneath it has become even more turbulent, mixing to an even greater extent high- and low-entropy matter. It is clear that, even in the presence of large-scale neutrino-driven convection, we do not, with our MGFLD neutrino transport, obtain an explosion.

In Figure 3b, we plot the one-dimensional entropy and two-dimensional angle-averaged entropy, both computed by the PPM code, as a function of radius at the same three time slices. The angle-averaged entropy is defined by

$$\langle S \rangle (i) = \frac{1}{A(i)} \sum_{j=1}^{n_\theta} A(i, j) S(i, j) \quad (4)$$

where

$$A(i, j) = 2\pi r^2(i) \sin \theta(j) d\theta \quad (5)$$

and where $A(i) = 4\pi r^2(i)$ and $d\theta = \pi/128$. At 137 ms after bounce, as expected, there is very little difference between the one- and two-dimensional profiles — convection has not yet fully developed and one would not expect large differences between the two simulations. At 212 ms after bounce, when convection has fully developed, it has clearly flattened the peak in the entropy profile between 90 and 150 km, relative to the one-dimensional case, and it is also clear that the shock location is a bit farther out — convection does seem to have an effect on the shock radius in our simulations, albeit marginal, pushing it out to slightly larger radii. Moreover, at this time, the maximum angle-averaged entropy is 13, which is not particularly high, nor even marginal for

an explosion. For example, Burrows *et al.* (1995) find that the entropies in their rising bubbles reach 25–35 prior to their explosions. Under explosive conditions, we expect entropies between the cooling protoneutron star and the shock to rise well past ~ 30 , a condition signaling the formation of a low-density radiation-dominated “bubble” behind the shock, as the shock separates itself from the protoneutron star. At the last time slice, 512 ms after bounce, the shock front is located at smaller radii, and the entropy jump across it is greater — the entropy behind the shock rises in time because the preshock matter density decreases and because the gravitational potential well becomes deeper, as more material accumulates onto the nascent neutron star and the radius of the shock decreases. The peak entropies for this last slice reach 17–18. In addition, the differences between our one- and two-dimensional simulations are less pronounced than at $t_{\text{pb}} = 212$ ms.

In Figure 4a, we show the two-dimensional electron fraction profiles at the same three postbounce times. These profiles are complementary to the entropy profiles. In particular, at $t_{\text{pb}} = 512$ ms we see low- Y_e (high-entropy) matter rising in dramatic expanding plumes, while high- Y_e (low-entropy) matter infalls in dense finger-like flows. The Y_e contrast between rising and falling flows is greatest at $t_{\text{pb}} = 137$ ms, when convection is developing and matter at disparate Y_e values in the Y_e profile beneath the shock, extending down to the trough near the neutrinospheres, is affected. In time, however, this contrast is lessened, and finally at $t_{\text{pb}} = 512$ ms, the matter in the neutrino-driven convection region has been sufficiently mixed that very little contrast is exhibited.

Figure 4b plots the angle-averaged electron fraction in our two-dimensional simulation against the corresponding one-dimensional results, both obtained with our PPM code. This quantity is defined by

$$\langle Y_e \rangle (i) = \frac{1}{A(i)} \sum_{j=1}^{n_\theta} A(i, j) Y_e(i, j) \quad (6)$$

No differences are seen near the Y_e trough, beneath the neutrino-driven convection region; all

differences occur directly below the shock, as expected. For example, a flattening in Y_e is evident between $t_{\text{pb}} = 137$ ms and $t_{\text{pb}} = 512$ ms, which is clearly seen in the region between 90 and 150 km at $t_{\text{pb}} = 212$ ms. In addition, in both one and two dimensions, the electron fraction gradient steepens as the shock recedes and high- Y_e matter advects inward through it. Similar to what we found in comparing the one- and two-dimensional entropy profiles, very little difference between our one- and two-dimensional electron fraction profiles is seen at the end of our simulation at $t_{\text{pb}} = 512$ ms.

In Figure 5a, we show the two-dimensional radial velocity profiles at $t = 137$, 212, and 512 ms after bounce. Comparing Figure 3a and 5a, high-velocity portions of the flow, accelerated by the buoyancy force, are associated both with inflow and with outflow. This is most easily seen looking at the second panel in both figures. The associations between the high inward radial velocity of the finger-like flow at $\theta \approx 60$ degrees and the high-velocity outflow associated with a portion of the rising plume at $\theta \approx 120$ degrees can easily be made. In Figure 5b, we plot the angle-averaged radial velocity from our two-dimensional run against the radial velocity from our 1D PPM run, as a function of time over our 500 ms window. The angle-averaged radial velocity is defined by

$$\langle v \rangle = \frac{1}{A(i)} \sum_{j=1}^{n_\theta} A(i, j) |v_r(i, j)| \quad (7)$$

The two profiles agree quite well before convection has fully developed at $t_{\text{pb}} = 137$ ms; differ most at $t_{\text{pb}} = 212$ ms, when convection is fully developed; and are in closer agreement at the end of our run at $t_{\text{pb}} = 512$ ms. When convection has had a chance to develop, the angle-averaged shock radius is farther out relative to the one-dimensional shock radius, but not significantly so. Moreover, in both simulations, the shock recedes and strengthens, as evidenced by the increased velocity jump across it at the end of our run. [In both our one- and two-dimensional simulations, there is a small periodic inward and outward movement of the shock, *i.e.*, a recession and a strengthening, followed by an advance and a weakening, and so on. As the shock moves out after strengthening, less material is advected onto the protoneutron star, and the accretion luminosity

drops. This decreases the neutrino heating behind the shock, thus undermining its pressure support, and the shock moves inwards. As the shock moves inwards, the accretion luminosity rises and the shock is once again strengthened, and moves out. This behavior has also been noted by others (*e.g.* , Mayle 1985).]

In Figure 6, we plot the angle-averaged radial and angular convection velocities in our two-dimensional run for the three postbounce slices we have focused on in this discussion, along with the angle-averaged sound speed. The convection velocities are defined by

$$\langle v_c \rangle_r = \frac{1}{A(i)} \sum_{j=1}^{n_\theta} A(i, j) |v_r(i, j)| - \langle v \rangle \quad (8)$$

and

$$\langle v_c \rangle_\theta = \frac{1}{A(i)} \sum_{j=1}^{n_\theta} A(i, j) |v_\theta(i, j)| \quad (9)$$

At the time when convection is fully developed, at $t_{\text{pb}} = 212$ ms, the radial convection velocities in our simulation become supersonic just below the shock. Notice, also, the anticorrelation between the radial and angular convection velocity profiles, which is consistent with the convective flow shown, for example, in Figure 3a. The radial convection velocity is at a minimum at the top of the convecting region where the matter turns over, at which point the angular convection velocity is at a maximum. At $t_{\text{pb}} = 512$ ms, the radial convection velocity is still supersonic just below the shock, despite the recession of the shock and the more turbulent convection.

For matter in nuclear statistical equilibrium, the thermodynamic state is completely determined once the density, temperature (or equivalently, entropy), and electron fraction are known. In Figures 3b and 4b, we have already graphed the angle-averaged entropy and electron fraction from our two-dimensional simulation, together with the corresponding profiles from our

one-dimensional MGFLD run. For completeness, in Figure 7 we plot the angle-averaged density. In the two-dimensional case, at $t_{\text{pb}} = 212$ and 512 ms, the shock is farther out in radius and the density jump therefore occurs at larger radii. Additionally, the shock is distorted in our two-dimensional simulation, and this gives the appearance in the angle-averaged density of shock smearing. Away from the shock, however, the one- and two-dimensional profiles are very nearly the same.

The neutrino heating rate (in MeV/nucleon) in the region between the neutrinospheres and the shock can be written as [see also equation (2)]

$$\dot{\epsilon} = \frac{X_n}{\lambda_0^a} \frac{L_{\nu_e}}{4\pi r^2} \langle E_{\nu_e}^2 \rangle \langle \frac{1}{\mathcal{F}} \rangle + \frac{X_p}{\bar{\lambda}_0^a} \frac{L_{\bar{\nu}_e}}{4\pi r^2} \langle E_{\bar{\nu}_e}^2 \rangle \langle \frac{1}{\bar{\mathcal{F}}} \rangle \quad (10)$$

where $X_{n,p}$ are the neutron and proton fractions; $\lambda_0^a, \bar{\lambda}_0^a$ are the coefficients of the $E_{\nu_e, \bar{\nu}_e}^{-2}$ neutrino-energy dependences in the electron neutrino and antineutrino mean free paths, respectively; $L_{\nu_e, \bar{\nu}_e}$, $\langle E_{\nu_e, \bar{\nu}_e}^2 \rangle$, and $\langle 1/\mathcal{F}, \bar{\mathcal{F}} \rangle$ are the electron neutrino and antineutrino luminosities, mean square energies, and mean inverse flux factors, respectively, as defined by

$$L_{\nu_e} = 4\pi r^2 \frac{2\pi c}{(hc)^3} \int dE_{\nu_e} d\mu_{\nu_e} E_{\nu_e}^3 \mu_{\nu_e} f \quad (11)$$

$$\langle E_{\nu_e}^2 \rangle = \frac{\int dE_{\nu_e} d\mu_{\nu_e} E_{\nu_e}^5 f}{\int dE_{\nu_e} d\mu_{\nu_e} E_{\nu_e}^3 f} \quad (12)$$

$$\langle \frac{1}{\mathcal{F}} \rangle = \frac{\int dE_{\nu_e} d\mu_{\nu_e} E_{\nu_e}^3 f}{\int dE_{\nu_e} d\mu_{\nu_e} E_{\nu_e}^3 \mu_{\nu_e} f} = \frac{cU_{\nu_e}}{F_{\nu_e}} \quad (13)$$

Corresponding quantities are similarly defined for the electron antineutrinos. In equations (11)–(13), f is the electron-neutrino distribution function, which is a function of the electron-neutrino

direction cosine, μ_{ν_e} , and energy, E_{ν_e} . In equation (13), U_{ν_e} and F_{ν_e} are the electron-neutrino energy density and flux. Success in generating explosions by neutrino heating must ultimately rest on these three key neutrino quantities. In Figures 8 and 9, we plot them at a radius of 1000 km, as a function of time during our simulation. Figure 8a shows the electron neutrino and antineutrino luminosities and RMS energies over the course of our entire simulation, whereas Figure 9 provides more detail over the crucial first 100 ms. The inverse flux factor is not plotted here because it is constant and unity at this radius. The luminosities and RMS energies at $r = 1000$ km are representative of the corresponding values in the gain region because they flatten out above the neutrinosphere radii. (For completeness, Figure 8b shows the muon and tau neutrino and antineutrino luminosities and RMS energies over the same period.)

Figure 10a gives the angle-averaged heating rate per gram as a function of radius at $t_{\text{pb}} = 137, 212, 512$ ms. The gain radius moves inward during this time, starting out at a radius of about 70 km and finishing up at a radius of about 55 km. Note also that as the gain radius moves inward, the shock also recedes, and the portion of the curve for which $\dot{\epsilon}$ is positive extends with time over a smaller radial region, *i.e.*, the gain volume decreases with time.

In Figure 10b we plot the maximum net heating and net cooling rates as a function of time during the course of our simulation. Figure 10c provides more detail over the first 150 ms. The drop and flattening in our net heating rate between the start of our run and 100 ms is consistent with the behavior exhibited by Janka and Müller (1996) in their Figure 13 for their exploding 2D model “T4c.” Between 50–100 ms, our net heating rate levels off at a value ~ 87 MeV/baryon/s, and the Janka and Müller rate levels off at a comparable though somewhat larger value ~ 93 MeV/baryon/s. However, the most dramatic difference between our results and theirs surfaces when comparing the magnitudes of the net cooling rate. Between 50–100 ms, our rate is ~ -193 MeV/baryon/s, whereas the Janka and Müller rate is 2–3 times less: ~ -75 MeV/baryon/s. Our dramatic increase in net cooling below the gain radius, resulting from our use of MGFLD, must account in large part for the lack of an explosion in our model despite the somewhat comparable net heating rate in the gain region, although Janka and Müller also begin with a larger initial shock

radius that results from starting their Newtonian simulation with one of our general relativistic postbounce models.

One final note: Equation (10) is appropriate for neutrino emission and absorption. In our simulation, the heating contributions from neutrino–electron scattering (NES) are negligible, amounting to 3–5% corrections for our postshock entropies ($\leq 17 - 18$). At typical postshock densities between 10^8 and 10^9 g/cm³, entropies ~ 30 (almost twice as large as our entropies) would be required before the number density of pairs would become comparable to the baryon number density, *i.e.*, before our NES heating contributions would double.

Figure 11 shows the evolution of the gain and shock radii in our one- and two-dimensional simulations. The shock follows the typical trajectory seen in all of our models: It moves out in radius to about 200 km in a quasihydrostatic way because of the rapid decline in the accretion ram pressure, and then recedes with some oscillation (most noticeably in the one-dimensional simulation) to a radius between 100–125 km at $t_{\text{pb}} = 500$ ms. Initially, the gain and shock radii diverge, giving rise to an increasingly larger gain region, but that trend reverses at $t_{\text{pb}} \approx 150$ ms. Note that, as a result of convection, the gain volume in our 2D simulation is larger than it is in our 1D simulation, but despite the increased gain volume, an explosion is not obtained.

More important, in Figures 12a and 12b, we plot the mass and internal energy in the gain region as a function of time during the course of our simulation. The initial rise in both mass and internal energy results primarily from the early dramatic increase in the gain volume, as the shock and gain radii diverge. However, at later times, both the gain region mass and internal energy decrease monotonically with time. This results because (1) the gain region is decreasing in size, and (2) the density ahead of the shock is falling off. The general trends exhibited by Figures 12a and 12b are indicative of a flow that passes through, rather than accumulates in, the gain region. Moreover, the ratio of the internal energy and mass in the gain region is roughly constant as a function of time, indicating that the total contributions to $\dot{\epsilon}$ in this region, from neutrino heating and cooling and from advection, cancel out.

4. Assessing Our Use of Precalculated 1D Neutrino Distributions

Our results depend in part on the assumption that our electron neutrino and antineutrino sources remain to a good approximation spherically symmetric during the course of our two-dimensional run. This requires that there be no significant convection in the region encompassing or below the neutrinospheres and no significant influence of neutrino-driven convection below the gain radii:

(A) *Convection Below the Neutrinospheres:* In a previous paper (Mezzacappa *et al.* 1997a), we presented compelling evidence that, in the presence of neutrino transport, the convective transport of heat and leptons below the neutrinospheres by protoneutron star convection will be significantly reduced. Our numerical results were supported by timescale analyses and by a simple analytical model, although final conclusions regarding the extent of protoneutron star convection await fully self-consistent multidimensional multigroup radiation hydrodynamics simulations. Nonetheless, these results are mentioned here in support of the conclusions reached in this paper. In the absence of significant protoneutron star convection, the imposition of a one-dimensional spherically-symmetric neutrino radiation field in the region between the neutrinospheres and the shock, used to compute the neutrino heating and cooling there, should be a good approximation.

(B) *The Influence of Neutrino-Driven Convection Below the Gain Radii:* Because our current prescription does not implement a self-consistent two-dimensional radiation hydrodynamics solution, we cannot capture enhancements in the neutrino luminosities emanating from the neutrinosphere region that result from (1) non-spherically-symmetric accretion through the gain radius and/or (2) inwardly propagating nonlinear waves that compress and heat the neutrinosphere region in a non-spherically-symmetric way. For example, the dense finger-like low-entropy inflows in the neutrino-driven convection region may penetrate the gain radius and strike the protoneutron star surface (Burrows *et al.* 1995, Janka & Müller 1996). It has been suggested that the associated luminosity enhancements may help trigger explosions (Burrows *et al.* 1995), but conclusions regarding their benefit have been mixed (Janka & Müller 1996).

To investigate whether these effects would have been important in our simulation, we compared our one- and two-dimensional density, temperature, and electron fraction snapshots at $t_{\text{pb}} = 212$ ms, *i.e.*, at a time when neutrino-driven convection was most vigorous. The results are represented graphically in Figure 13. Up to the neutrinosphere radii (~ 51 km), we found no differences. Between the neutrinospheres and the gain radii (~ 90 km), we found hot spots in our two-dimensional simulation where $\Delta T/T \sim 3\%$ over $\sim 1/8$ – $1/6$ of the volume and $\sim 6\%$ over $\sim 1/8$ – $1/6$ of the volume, and Y_e -enhanced spots where $\Delta Y_e/Y_e \sim 9\%$ over $\sim 1/4$ – $1/3$ of the volume. However, at $t \sim 100 - 200$ ms after bounce, $L_{\nu_e}(50 \text{ km}) \approx 2.4 \times 10^{52}$ erg/s and $L_{\nu_e}(90 \text{ km}) \approx 3.4 \times 10^{52}$ erg/s; therefore, only $\sim 33\%$ of the neutrino luminosities would have been affected by these temperature and electron-fraction enhancements. (The percentages for electron antineutrinos are comparable: $\sim 50\%$ at 100 ms and $\sim 33\%$ at 200 ms.) We also considered the enhancements to the electron neutrino and antineutrino pair emissivity due to the hot spots, because of its strong (T^9) dependence on the local matter temperature. In our model the pair emissivity contributes only $\sim 10\%$ to the total electron neutrino and antineutrino emissivity. The hot spots would increase this contribution, but only to $\sim 15\%$ of the total emissivity.

Considering the small local enhancements in T and Y_e , the small percentage of the volume in which they occur, and the fraction of the neutrino luminosities that would be affected by them, we do not expect these enhancements to have significant ramifications for the supernova outcome.

5. Summary, Comparisons, and Conclusions

With two-dimensional (PPM) hydrodynamics “coupled” to one-dimensional MGFLD neutrino transport, we see vigorous — in some regions supersonic — neutrino-driven convection develop behind the shock. Despite this, we do not obtain explosions for what should be an “optimistic” $15 M_{\odot}$ model. Beginning with realistic postbounce initial conditions, our simulation has been carried out for ~ 500 ms, a period that is long relative to the 50–100 ms explosion timescales obtained by other groups, for models that explode.

An important and very interesting feature of our two-dimensional model is that, even in the presence of neutrino-driven convection, the angle-averaged density, entropy, electron fraction, and radial velocity do not differ very much from their counterparts in our accompanying one-dimensional MGFLD run. The differences arise primarily because convection in our two-dimensional simulation has moved the shock somewhat farther out in radius. This indicates that, while vigorous convection may be present, it does not contribute in our models in any significant way to the angle-averaged shock dynamics.

The differences in outcome from group to group, and even from model to model for a given group, most likely result in large part from several factors: (1) Differences between numerical hydrodynamics methods, in particular, SP and PPM hydrodynamics, most likely contribute. With PPM hydrodynamics, neutrino-driven convection is more turbulent, and consequently, the separation between high- and low-entropy matter in the gain region, exhibited in the Herant *et al.* simulations, does not obtain. This may have an impact on the neutrino heating efficiency, as discussed by Herant *et al.* in proposing their “Carnot engine” interpretation of the supernova mechanism. (Although we again note that Miller *et al.* found low-mode convection, but not a “Carnot engine.”) (2) As stressed in Bruenn and Mezzacappa (1994), it is important to begin any 2D simulation with initial postbounce conditions that have been generated by realistic core collapse and bounce, which necessitates the use of neutrino transport that includes all relevant neutrino interactions, particularly neutrino-electron scattering (NES). NES is known to have a significant effect on the deleptonization of the core during infall, and consequently, on the location

and strength of the shock after bounce. We begin our simulations with postbounce configurations that have been evolved through collapse and bounce with MGFLD, and NES included. In Figure 5a of Burrows *et al.* (1995), the early shock trajectory behaves like an initially stronger “prompt” shock. In contrast, in our simulations the shock moves out quasihydrostatically as a result of the accretion of matter through it. The greater initial shock strength in the Burrows *et al.* simulation most likely results from the difference between simulating core collapse with a neutrino leakage scheme (Burrows and Lattimer 1986), as opposed to MGFLD (Bruenn 1985). For the simulations presented in Herant *et al.* (1994), the same gray transport scheme is used both for their 1D core collapse evolution and their 2D postbounce evolution. It would be enlightening to investigate the differences in postbounce conditions, and in particular, shock location and strength, obtained using gray and multigroup transport during core collapse and bounce. It is also important to stress that we use a 1D Newtonian postbounce profile to start our 2D Newtonian simulations. For Janka and Müller (1996), the initial shock radius increased from ~ 120 km to ~ 200 km, *i.e.*, by nearly a factor of 2, because they started their 2D Newtonian simulation with our 1D general relativistic postbounce model. This initial boost in shock radius will have an effect on the subsequent shock trajectory. (3) Ultimately, success or failure in generating supernova explosions rests on the right combination of neutrino luminosities, RMS energies, and inverse flux factors. Whereas it is possible to list a number of inputs that might differ from group to group, and within each group, from simulation to simulation, the one that stands out the most is the neutrino RMS energy. Of course, the neutrino heating rate depends on the square of the neutrino RMS energy; therefore, differences in this quantity are magnified when folded into the final heating rate. For example, we find that with the Burrows *et al.* (1995) specification of both T_{ν_e} and η_{ν_e} , the relationship between their neutrinosphere temperature and neutrino RMS energy for their exploding “star” model is $\langle E_{\nu_e}^2 \rangle^{1/2} = 3.6T_{\nu_e}$. When we fit our electron neutrino spectrum at our neutrinosphere radius, we obtain a characteristic dependence on temperature of $3.0T_{\nu_e}$. This difference translates to a 40–50% increase in the neutrino heating rate for the Burrows *et al.* “star” model, with commensurate ramifications for generating explosions. Burrows *et al.* note that explosions are not obtained in other models, presumably when the values of T_{ν_e} and η_{ν_e} are

chosen differently. Similarly, our mean electron neutrino and antineutrino energies, relative to those given by Herant *et al.* (1994) for their 25 M_{\odot} model in their Figure 10, are significantly lower. At 100 ms after bounce, our mean electron neutrino and antineutrino energies are 10 and 13 MeV, respectively, compared with the 13–14 and ~ 20 MeV values obtained by Herant *et al.* The differences between our results and the results obtained by the two groups mentioned above result from: (1) specification (Burrows *et al.*) rather than computation of the neutrino spectra in optically thin regions; (2) patching together optically thick and thin regions, rather than having a transport scheme that transits through both regions. The maximum net heating rates obtained by Janka and Müller (1996) between their gain radii and shock are comparable to but somewhat higher than ours: ~ 93 MeV/baryon/s, versus ~ 87 MeV/baryon/s; however, their maximum net cooling rates below their gain radii are 2–3 times lower than ours: ~ -75 MeV/baryon/s, versus ~ -193 MeV/baryon/s. The MGFLD treatment we use gives a much greater neutrino cooling rate in deeper regions, which, as is well known, undermines efforts to generate explosions (*e.g.* , see Herant *et al.* 1992).

We have computed the mass and internal energy in the gain region as a function of time to address the issue of whether or not neutrino-driven convection leads to greater neutrino heating efficiency and the accumulation of mass and energy in the gain region [Bethe (1990), Herant *et al.* (1994)]. Other interpretations suggest that supernovae result as critical phenomena when the neutrino luminosities are sufficiently high, given the ram pressure of the preshock matter, to render the flow unstable to explosion [Burrows and Goshy (1993), Burrows *et al.* (1995)]. We find an increase in mass and internal energy in the gain radius up to about 150 ms after bounce, as a result of the increasing gain volume as the gain and shock radii diverge. After that, we find a monotonic decrease in both quantities, consistent with the density falloff in the preshock matter and with matter flowing through, rather than accumulating in, the gain region.

To assess our use of precalculated 1D neutrino distributions for matter heating and deleptonization, we have considered the non-spherically-symmetric luminosity enhancements that would occur from local temperature and electron fraction enhancements below the gain radii

(which enclose the electron neutrino and antineutrino sources) that are seen in our two-dimensional run, which result either from non-spherically-symmetric accretion through the gain radius or nonlinear inwardly propagating non-spherically-symmetric waves. We see no enhancements below the neutrinosphere radii; between them and the gain radii, we see small enhancements that occur over a small fraction of the volume responsible for producing less than 1/3 of the neutrino luminosities. Therefore, we do not expect these enhancements to have dynamical consequences.

We do not expect to obtain explosions for more massive stars. Moreover, our simulations are Newtonian. With general relativistic gravity, conditions will be even more pessimistic. The neutrino luminosities will be redshifted, the increased infall velocities and the smaller width between the gain radii and the shock will allow less time for neutrino heating to reverse infall, and everything will occur in a deeper gravitational well, making explosion more difficult.

We are in the process of carrying out simulations with ray-by-ray MGFLD coupled to two-dimensional hydrodynamics in an effort to (1) “bracket” the approximation of using one-dimensional neutrino transport in a two-dimensional setting and (2) step toward a two-dimensional multigroup neutrino transport scheme. The imposition of spherical symmetry in our current model maximizes the lateral transport of neutrinos in regions that are optically thick, which would have a tendency to minimize convection in that region (Mezzacappa *et al.* 1997a); whereas ray-by-ray transport, by definition, minimizes it. Our results regarding neutrino-driven convection in the gain region hinge on our assumption that the neutrino radiation field there is realistically determined by one-dimensional MGFLD neutrino transport in the region near and below the neutrinospheres. (Otherwise, our use of 1D precalculated distributions would not be a good approximation.) “Bracketing” our one-dimensional neutrino transport approximations will give us a better sense of how realistic these approximations are. Of course, final conclusions regarding our 1D transport approximations await fully self-consistent two-dimensional multigroup radiation hydrodynamics simulations.

On a more optimistic note, recently we have obtained new results from comparisons of three-flavor Boltzmann neutrino transport and three-flavor MGFLD in postbounce supernova

environments (thermally frozen, hydrostatic). In particular, the Boltzmann net heating rate in the region directly above the gain radii is significantly larger (Mezzacappa *et al.* 1997b). These results suggest that Boltzmann transport will yield greater neutrino heating and more vigorous neutrino-driven convection; both would increase the chances of reviving the stalled shock.

Finally, it is well known that in two and three dimensions energy cascades in different directions, from short- to long-wavelength modes in two dimensions, and in the opposite direction in three dimensions (Porter, Pouquet, & Woodward 1992). Consequently, we expect three-dimensional simulations to “look” more like one-dimensional simulations than do our two-dimensional simulations. Therefore, it may be more, not less, difficult to obtain explosions in 3D, if success in generating explosions relies heavily on convection. We are currently investigating the dependence of neutrino-driven convection on the number of spatial dimensions (Knerr *et al.* 1997). To make matters worse, ultimately we will have the task of obtaining general relativistic 3D explosions, with or without the aid of convection, and if one considers other complexities, like (1) the uncertainties in the precollapse models, high-density equation of state [*e.g.*, see Keil & Janka (1995)], and high-density neutrino opacities [*e.g.*, see Raffelt and Seckel (1994)], and (2) the noninclusion of rotation [*e.g.*, see Shimizu *et al.* (1994)] and other potentially important input physics in simulations that include realistic multidimensional hydrodynamics and neutrino transport, we are far from being able to say definitively how supernovae explode and whether or not a single component of the problem, like convection, is the key to unlocking it.

6. Acknowledgements

AM, ACC, MWG, and MRS were supported at the Oak Ridge National Laboratory, which is managed by Lockheed Martin Energy Research Corporation under DOE contract DE-AC05-96OR22464. AM, MWG, and MRS were supported at the University of Tennessee under DOE contract DE-FG05-93ER40770. ACC and SU were supported at Vanderbilt University under DOE contract DE-FG02-96ER40975. SWB was supported at Florida Atlantic University under NSF grant AST-9618423 and NASA grant NRA-96-04-GSFC-073, and JMB was supported at North Carolina State University under NASA grant NAG5-2844. The simulations presented in this Letter were carried out on the Cray C90 at the National Energy Research Supercomputer Center, the Cray Y/MP at the North Carolina Supercomputer Center, and the Cray Y/MP and Silicon Graphics Power Challenge at the Florida Supercomputer Center. We would like to thank Willy Benz, Adam Burrows, Chris Fryer, Wolfgang Hillebrandt, Thomas Janka, Ewald Müller, Michael Smith, Doug Swesty, and Friedel Thielemann for stimulating discussions; and especially the referee, Stirling Colgate, for many important comments, questions, and suggestions that improved the content of this paper significantly.

7. References

- Arnett, W. D. 1986, in IAU Symposium 125, The Origin and Evolution of Neutron Stars, ed. D. J. Helfand and J. H. Huang (Dordrecht: Reidel)
- Arnett, W. D. 1987, *ApJ*, 319, 136
- Arnett, W. D., Fryxell, B., & Müller, E. 1989, *ApJ*, 341, L63
- Bethe, H. A. 1990, *Rev. Mod. Phys.*, 62, 801
- Bethe, H. A. 1993, *ApJ*, 412, 192
- Bethe, H. A., Brown, G. E., & Cooperstein, J. 1987, *ApJ*, 322, 201
- Bethe, H. & Wilson, J. R. 1985, *ApJ*, 295, 14
- Bowers, R. L., & Wilson, J. R. 1991, *Numerical Modeling in Applied Physics and Astrophysics* (Boston: Jones & Bartlett), chap. 5
- Bruenn, S. W. 1993, in *Nuclear Physics in the Universe*, eds. M. W. Guidry and M. R. Strayer (IOP Publishing, Bristol), p. 31
- Bruenn, S. W. & Mezzacappa, A. 1994, *ApJ*, 433, L45
- Bruenn, S. W., Mezzacappa, A., & Dineva, T. 1995, *Phys. Rep.*, 256, 69
- Bruenn, S. W. & Dineva, T. 1996, *ApJ*, 458, L71
- Burrows, A. 1987, *ApJ*, 318, L63
- Burrows, A. & Lattimer, J. M. 1988, *Phys. Rep.*, 163, 5
- Burrows, A., Hayes, J., & Fryxell, B. A. 1995, *ApJ*, 450, 830
- Burrows, A. & Fryxell, B. A. 1992, *Science*, 258, 430
- Burrows, A. & Fryxell, B. A. 1993, *ApJ*, 418, L33
- Colella, P., & Woodward, P. 1994, *J. Comp. Phys.*, 54, 174

- Colgate, S. A., & White, R. H. 1966, *Ap. J.*, 143, 626
- Colgate, S. A., Herant, M. E., & Benz, W. 1993, *Phys. Rep.*, 227, 157
- Cook, W. R., *et al.* 1988, *ApJ*, 334, L87
- Cooperstein, J. 1993, in *Nuclear Physics in the Universe*, eds. M. W. Guidry and M. R. Strayer (IOP Publishing, Bristol), p. 99
- Den, M., Yoshida, T., & Yamada, Y. 1990, *Progr. Theor. Phys.*, 83, 723
- Dotani, T., *et al.* 1987, *Nature*, 330, 230
- Epstein, R. I. 1979, *MNRAS*, 188, 305
- Erikson, E. F., Hass, M. R., Colgan, S. W. J., Lord, S. D., Burton, M. G., Wolf, J., Hollenbach, D. J., & Werner, H. 1988, *ApJ*, 330, L39
- Fryxell, B., Arnett, W. D., & Müller, E. 1991, *ApJ*, 367, 619
- Gehrels, N., MacCallum, C. J., & Leventhal, M. 1987, *ApJ*, 320, L19
- Gehrels, N., Leventhal, M., & MacCallum, C. J. 1988, in *Nuclear Spectroscopy of Astrophysical Sources*, ed. N. Gehrels & G. Share (New York: AIP), p. 87
- Haas, M. R., Colgan, S. W. J., Erickson, E. F., Lord, S. D., Burton, M. G., & Hollenbach, D. J. 1990, *ApJ*, 360, 257
- Hachisu, I., Matsuda, T., Nomoto, K., Shigeyama, T. 1990, *ApJ*, 358, L57
- Herant, M., & Benz, W. 1991, *ApJ*, 370, L81
- Herant, M., & Benz, W. 1992, *ApJ*, 387, 294
- Herant, M., Benz, W., & Colgate, S. A. 1992, *ApJ*, 395, 642
- Herant, M., Benz, W., Hix, W. R., Fryer, C. L., & Colgate, S. A. 1994, *ApJ*, 435, 339
- Höflich, O. 1988, in *IAU Colloq. 108, Atmospheric Diagnostics of Stellar Evolution*,

- ed. K. Nomoto (Berlin: Springer), p. 288
- Janka, H.-Th. & Müller, E. 1993a, in Proc. of the IAU Coll. 145 (Xian China, May 24-29, 1993), eds. R. McCray and Wang Zhenru, (Cambridge Univ. Press, Cambridge); MPA-Preprint 748
- Janka, H.-Th. & Müller, E. 1993b, in Frontiers of Neutrino Astrophysics, eds. Y. Suzuki and K. Nakamura, (Universal Academy Press, Tokyo). p. 203
- Janka, H.-Th. & Müller, E. 1995, Ap. J., 448, L109
- Janka, H.-Th., & Müller, E. 1996, A&A 306, 167
- Keil, W. & Janka, H.-Th. 1995, A&A, 296, 145
- Keil, W., Janka, H.-Th, & Müller, E. 1996, ApJ, 473, L111
- Knerr, J., Blondin, J. M., Mezzacappa, A., and Bruenn, S. W. 1997, in preparation
- Mahoney, W. A., *et al.* 1988, ApJ, 334, L81
- Matz, S. M., Share, & Chupp, E. L., 1988, in Nuclear Spectroscopy of Astrophysical Sources, ed. N. Gehrels & G. Share (New York: AIP)
- Matz, S. M., Share, G. H., Leising, M. D., Chupp, E. L., Vestrand, W. T., Purcell, W. R., Strickman, M. S., & Reppin, C. 1988, Nature, 331, 416
- Mayle, R. W. 1985, Ph.D. Thesis, Univ. California, Berkeley (UCRL preprint no. 53713)
- McCray, R., Shull, J. M., & Sutherland, P. 1988, ApJ, 327, L73
- Mezzacappa, A., Messer, O. E. B., Bruenn, S. W., & Guidry, M. W. 1997b, in preparation
- Mezzacappa, A., Calder, A. C., Bruenn, S. W., Blondin, J. M., Guidry, M. W., Strayer, M. R., & Umar, A. S. 1997a, ApJ, in press
- Miller, D. S., Wilson, J. R., & Mayle, R. W. 1993, ApJ, 415, 278
- Müller, E. 1993, in Proc. of the 7th Workshop on Nuclear Astrophysics (Ringberg

- Castle, March 22-27, 1993), eds. W. Hillebrandt and E. Müller, Report MPA/P7, Max-Planck-Institut für Astrophysik, Garching, p. 27
- Müller, E. & Janka, H.-Th. 1994, in Reviews in Modern Astronomy 7 (Proc. of the Int. Conf. of the AG (Bochum, Germany, 1993)), eds. G. Klure (Astronomische Gesellschaft, Hamburg), p. 103
- Müller, E., Fryxell, B., & Arnett W. D. 1991, in Proc. Elba Workshop on Chemical and Dynamical Evolution of Galaxies, ed. F. Federini, J. Franco, & F. Matteucci (Pisa: ETS Editrice), p. 394
- Pinto, P. A., & Woosley, S. E. 1988, *Nature*, 333, 534
- Porter, D. H., Pouquet, A., & Woodward, P. R. 1992, *Theor. Comput. Fluid Dynamics*, 4, 13
- Raffelt, G., & Seckel D. 1994, *Phys. Rev. D*, to be published
- Rank, D. M., *et al.* 1988, *Nature*, 331, 505
- Sandie, W. G., *et al.* 1988, *ApJ*, 334, L91
- Shimizu, T., Yamada, S., & Sato, K. 1994, *ApJ*, 432, L119
- Spyromilio, J., Meikle, W. P. S., & Allen, D. A. 1990, *MNRAS*, 242, 669
- Sunyaev, R., *et al.* *Nature*, 330, 227
- Teegarden, B. J., *et al.* 1989, *Nature*, 339, 122
- Tuller, J., Barthelemmy, S., Gehrels, N., Teegarden, B. J., Leventhal, M., & MacCallum, C. J. 1990, *ApJ*, 351, L41
- Weaver, T. A. & Woosley, S. E. 1997, *ApJ*, in preparation
- Wilson, J. R. 1985, in Numerical Astrophysics, eds. J. M. Centrella, J. M. LeBlanc, & R. L. Bowers (Boston: Jones & Bartlett), p. 422

Wilson, J. R. & Mayle, R. W. 1988, *Phys. Rep.*, 163, 63

Wilson, J. R. & Mayle, R. W. 1993, *Phys. Rep.*, 227, 97

Wilson, R. B., *et al.* 1988, in *Nuclear Spectroscopy of Astrophysical Sources*, ed. N. Gehrels & G. Share (New York: AIP), p. 66

Woosley, S. E. & Weaver, T. A. 1995, *ApJS*, 101, 181

Xu, Y., Sutherland, P., McCray, R., & Ross, R. 1988, *ApJ*, 327, 197

Yamada, Y., Nakamura, T., & Oohara, K. 1990, *Progr. Theor. Phys.*, 84, 436

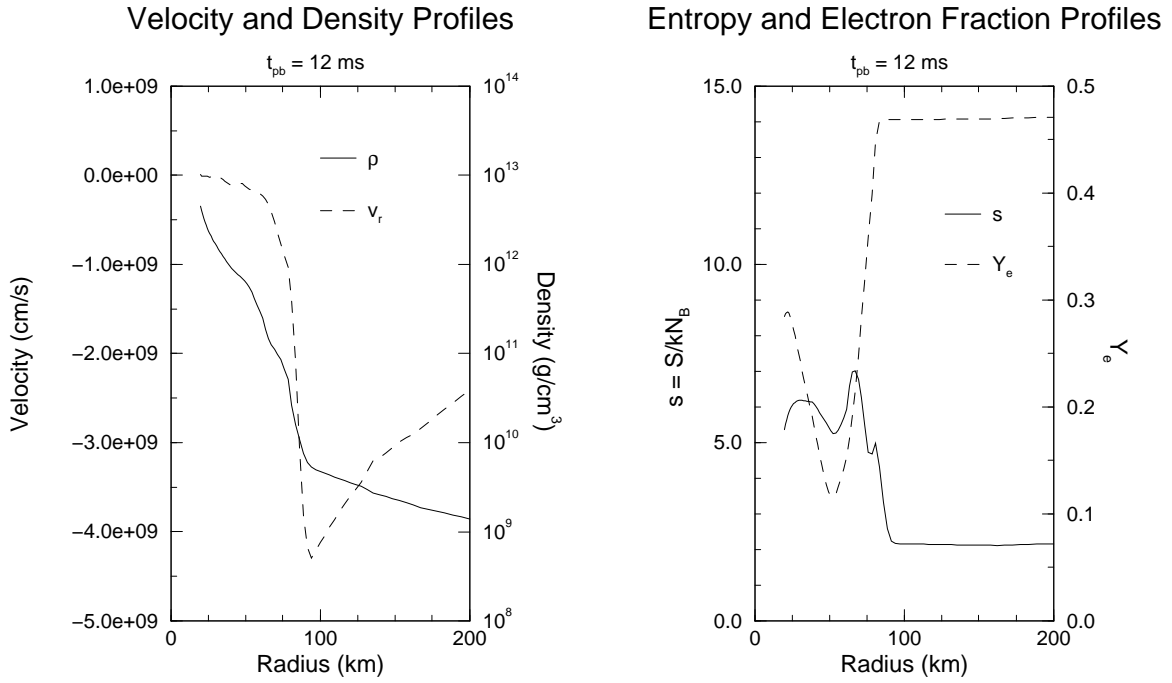


Fig. 1.— Initial postbounce velocity, density, entropy, and electron fraction profiles for our 15 M_⊙ model.

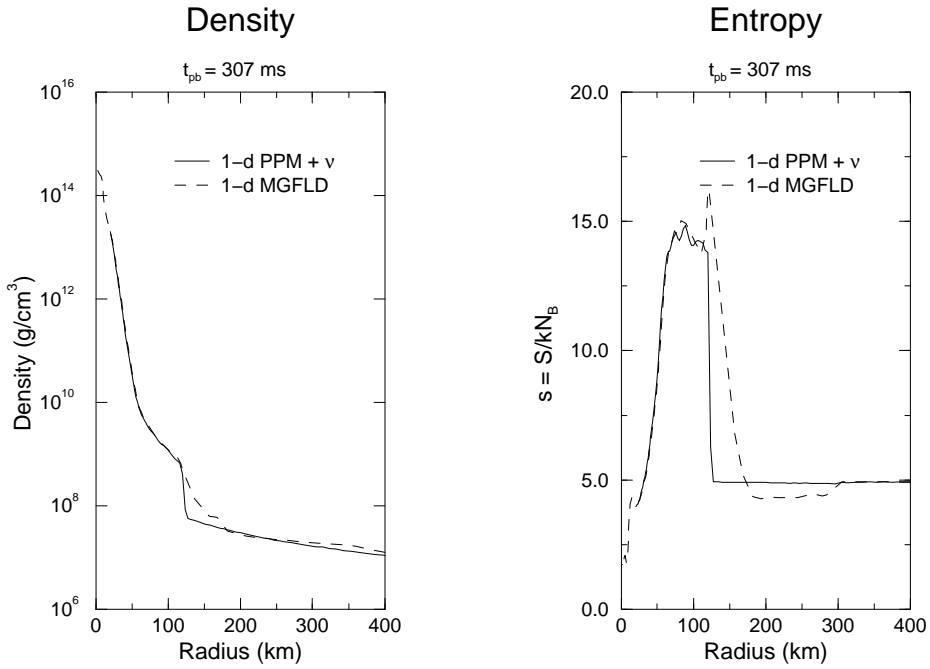


Fig. 2a.— Plots of density and entropy versus radius comparing one-dimensional simulations with our PPM and MGFLD codes, at 307 ms after the start of our run.

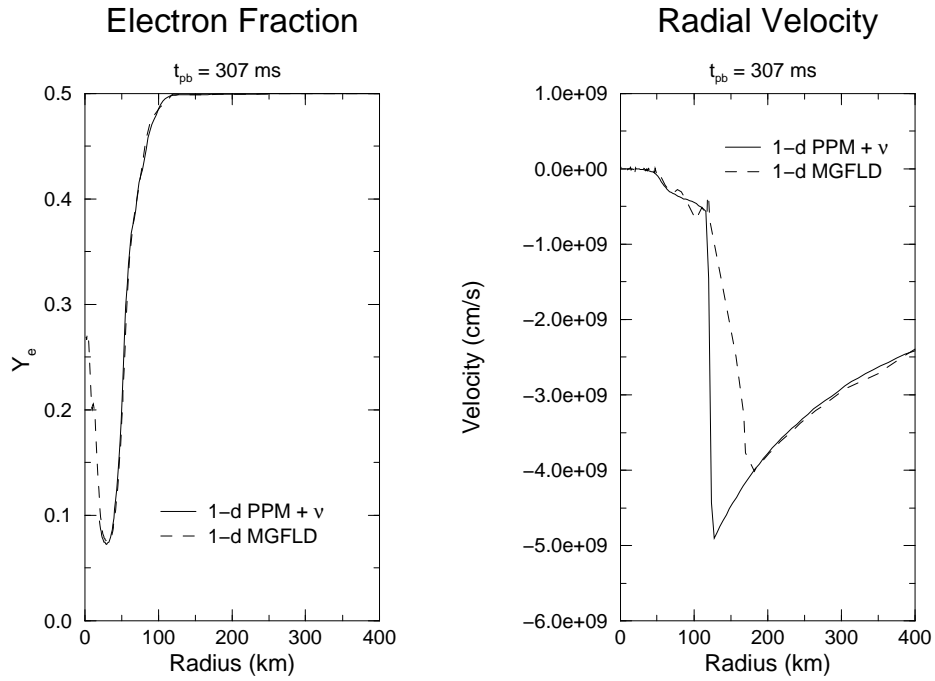


Fig. 2b.— Plots of electron fraction and radial velocity versus radius for the same comparison shown in Figure 2a.

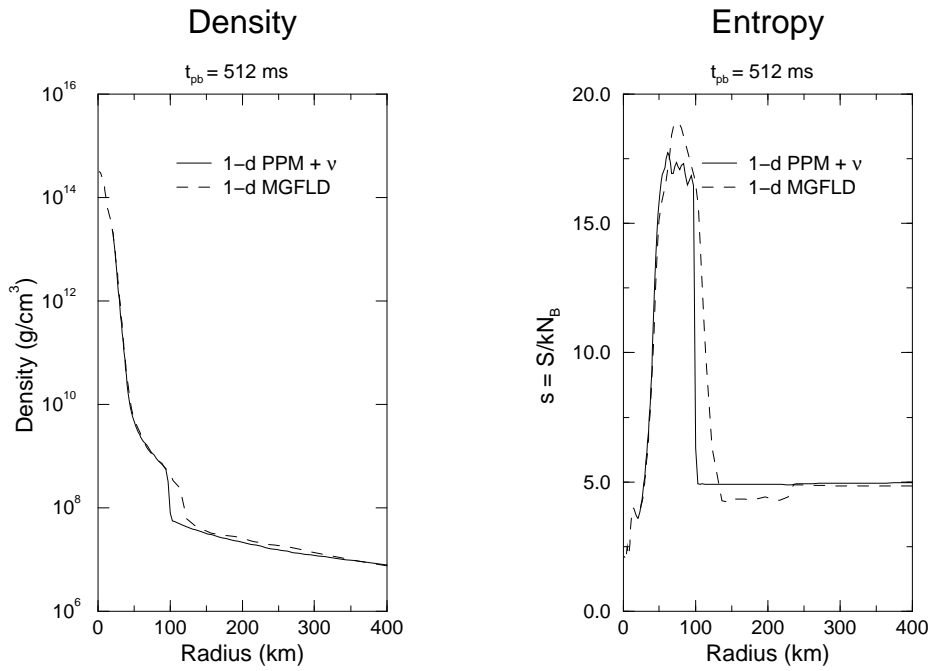


Fig. 2c.— Plots of density and entropy versus radius comparing one-dimensional simulations with our PPM and MGFLD codes, at 512 ms after the start of our run.

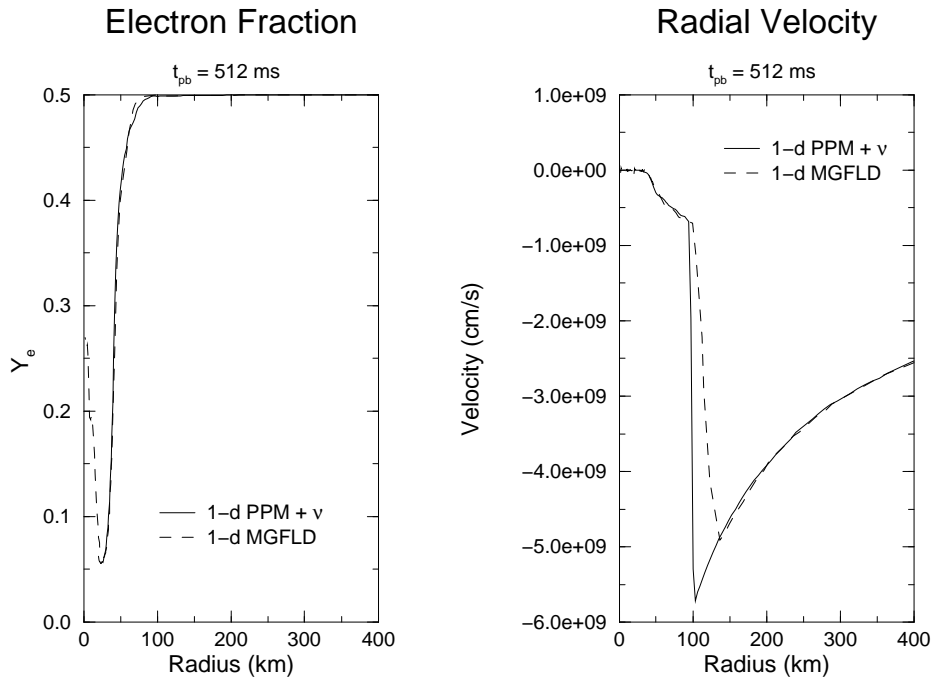


Fig. 2d.— Plots of electron fraction and radial velocity versus radius for the same comparison shown in Figure 2c.

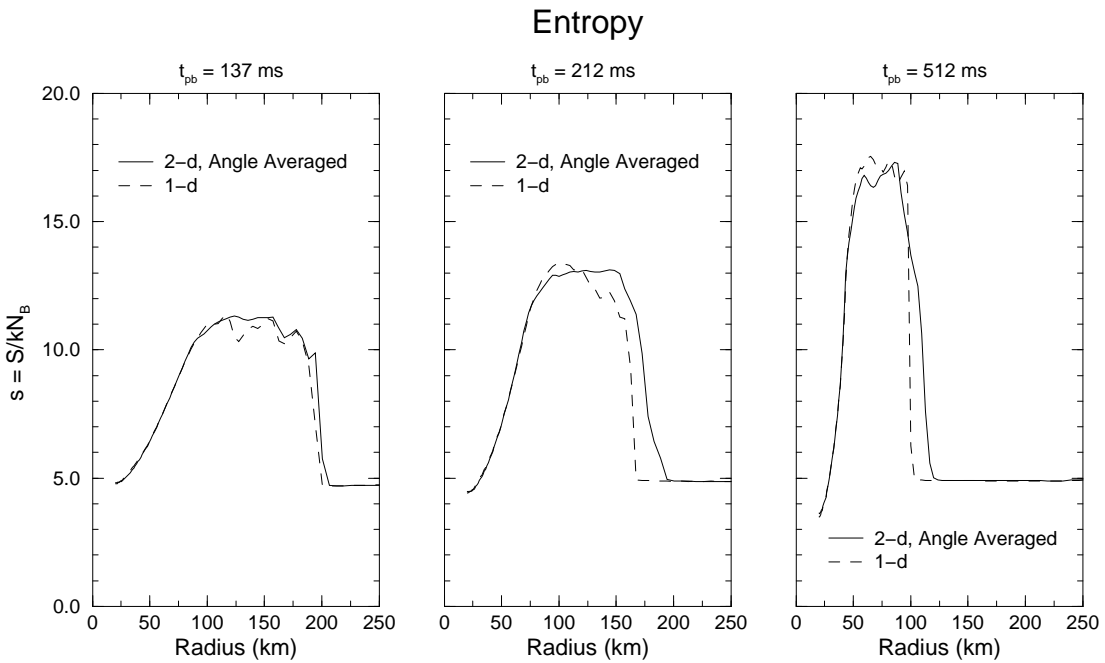


Fig. 3b.— Plots of the angle-averaged entropy for the three entropy snapshots shown in Figure 3a. Also shown for comparison are the corresponding entropy profiles from our 1D PPM simulation.

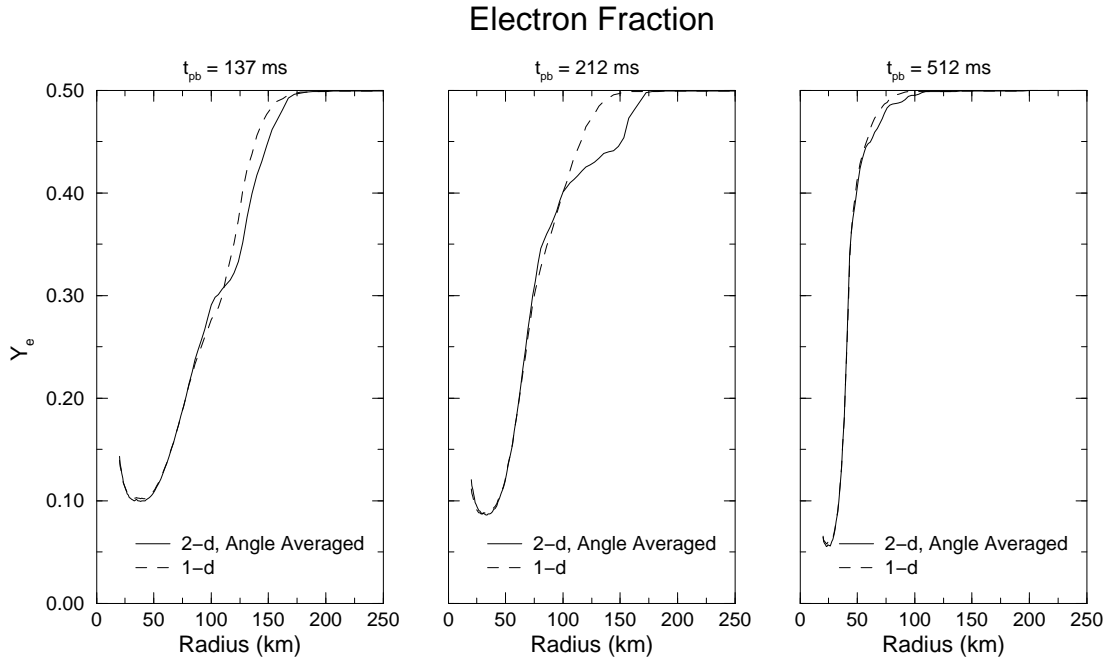


Fig. 4b.— Plots of the angle-averaged electron fraction for the three electron fraction snapshots shown in Figure 4a. Also shown for comparison is the corresponding electron fraction from our 1D PPM simulation.

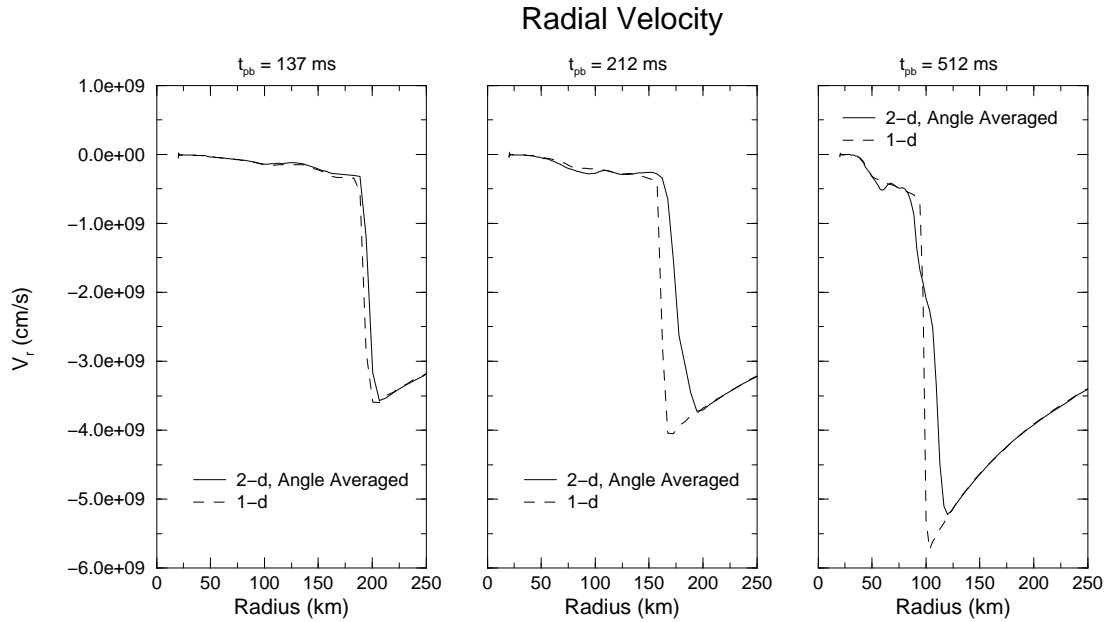


Fig. 5b.— Plots of the angle-averaged radial velocity for the three radial velocity snapshots shown in Figure 4a. Also shown for comparison is the corresponding radial velocity from our 1D PPM simulation.

Convection Velocities

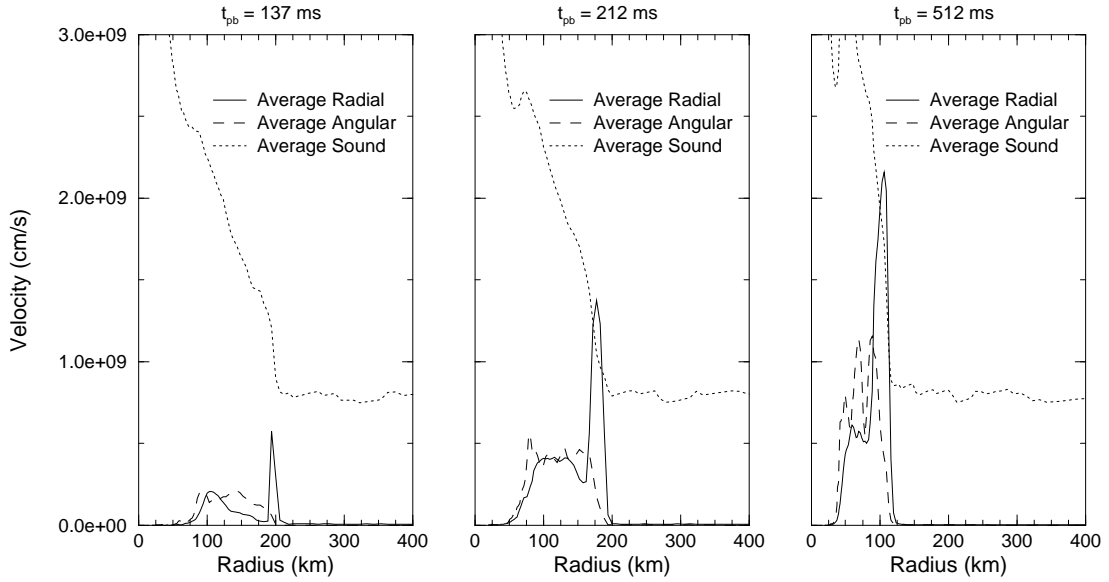


Fig. 6.— Plots of the angle-averaged radial convection velocity, angular convection velocity, and local sound speed at 137, 212, and 512 ms after bounce.

Density

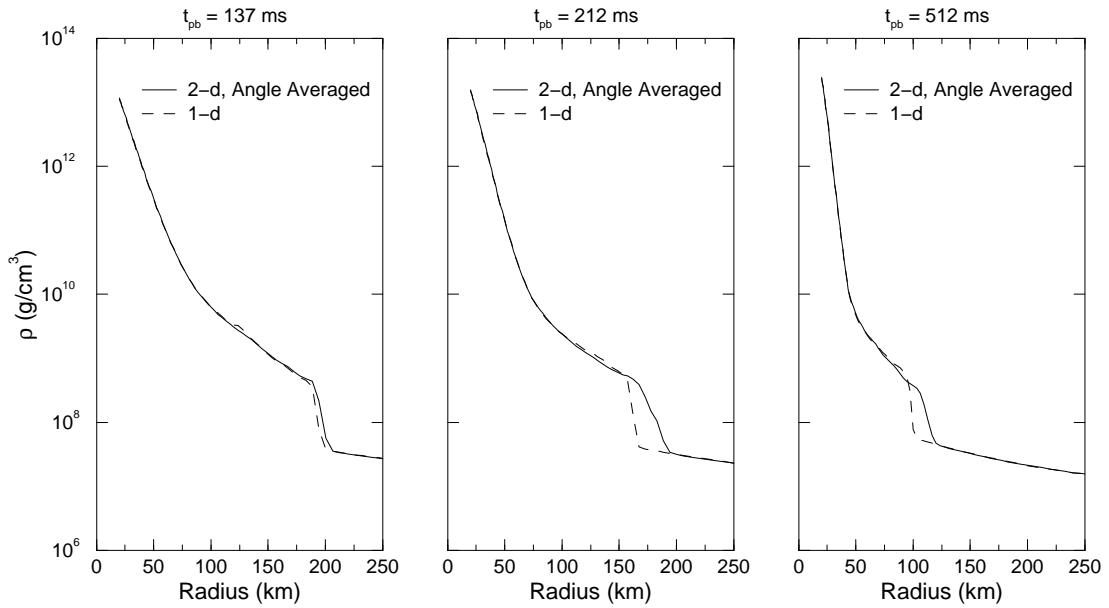


Fig. 7.— Plots of the angle-averaged density at 137, 212, and 512 ms after bounce. Also shown for comparison is the corresponding density from our 1D PPM simulation.

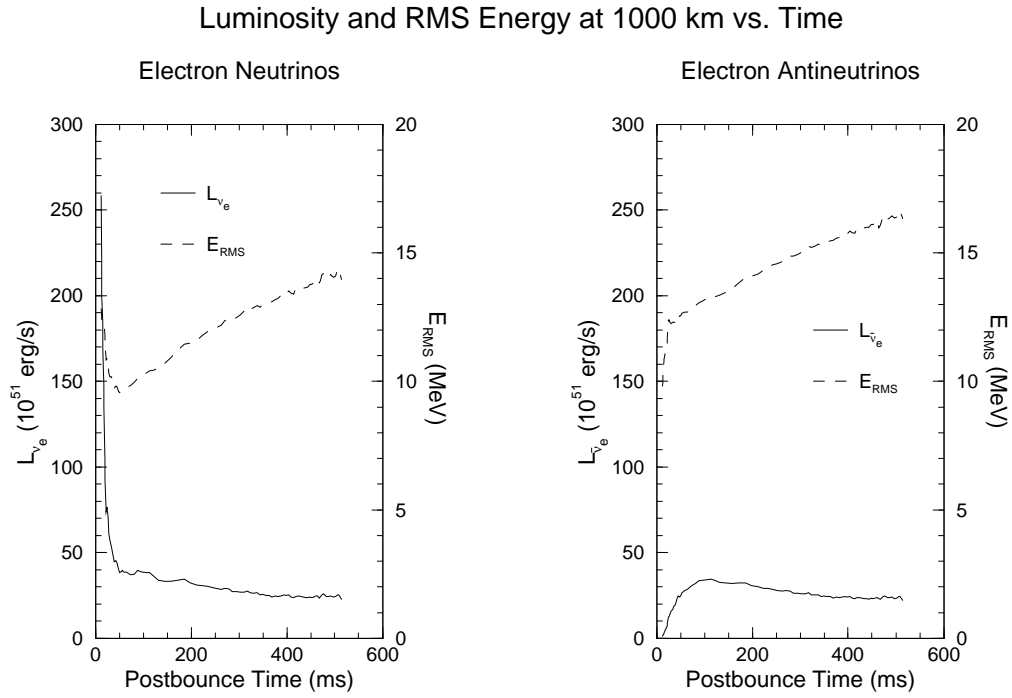


Fig. 8a.— Plot of the MGFLD electron neutrino and antineutrino luminosities and RMS energies at 1000 km, as a function of time.

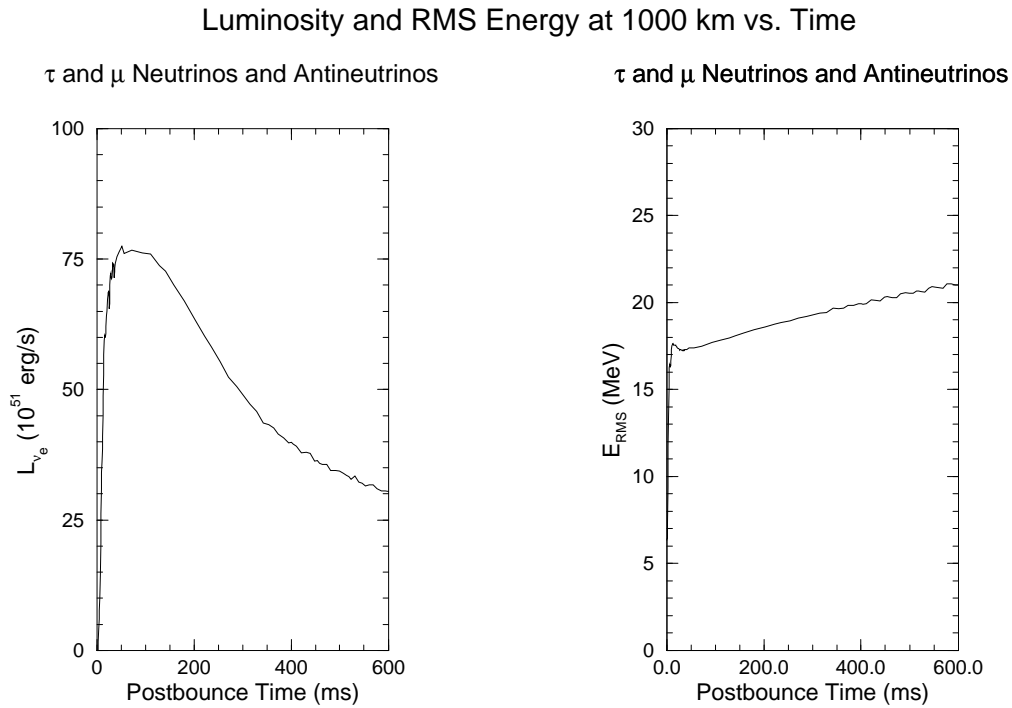


Fig. 8b.— Plot of the MGFLD muon and tau neutrino and antineutrino luminosities and RMS energies at 1000 km, as a function of time.

Luminosity and RMS Energy at 1000 km vs. Time

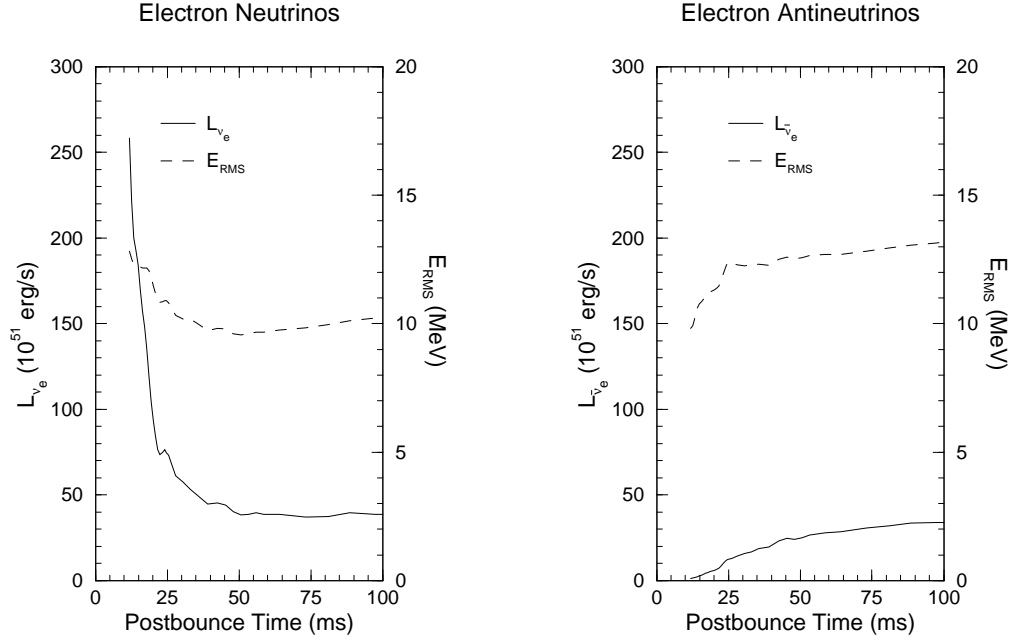


Fig. 9.— Early detail of the MGFLD electron neutrino and antineutrino luminosities and RMS energies at 1000 km.

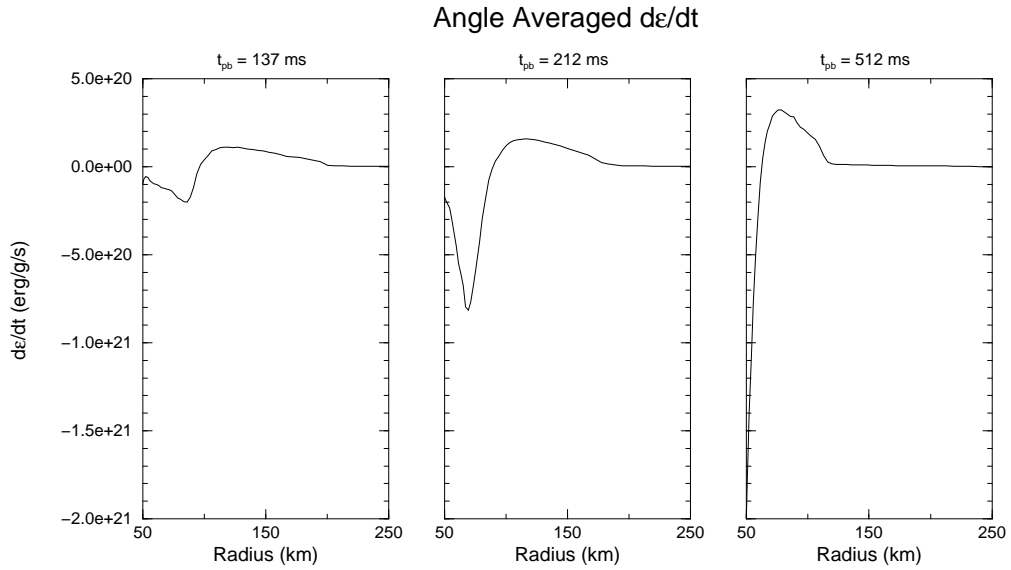


Fig. 10a.— Plots of the angle-averaged $d\epsilon/dt$ at 137, 212, and 512 ms after bounce. $d\epsilon/dt$ is the net heating or cooling due to electron neutrino and antineutrino absorption and emission.

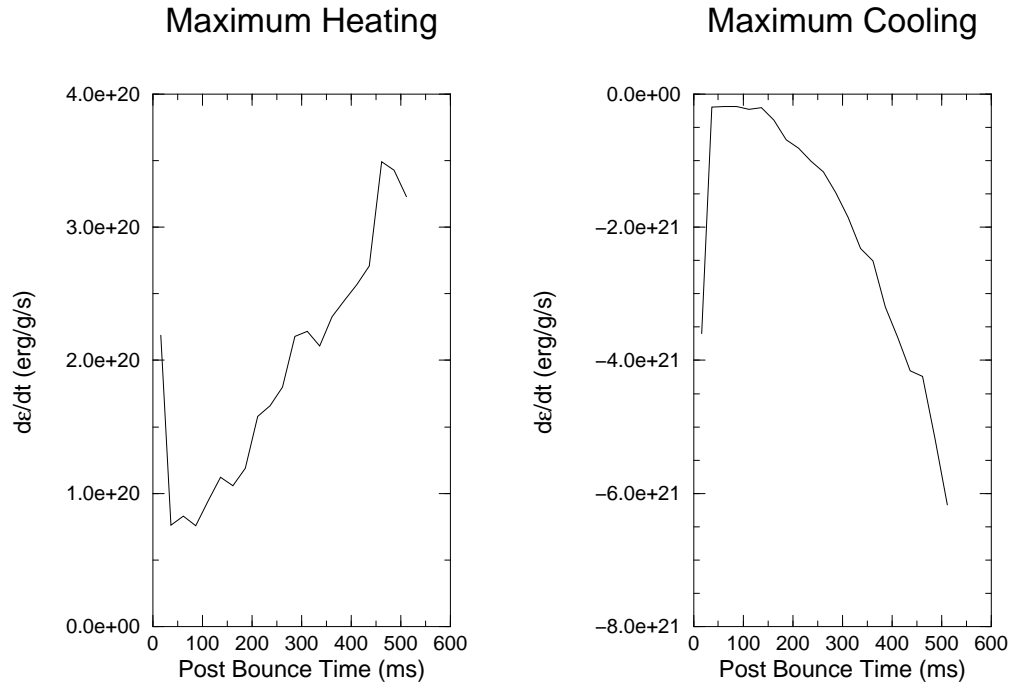


Fig. 10b.— Plots of the maximum net neutrino heating and net neutrino cooling rates as a function of time during the course of our simulation.

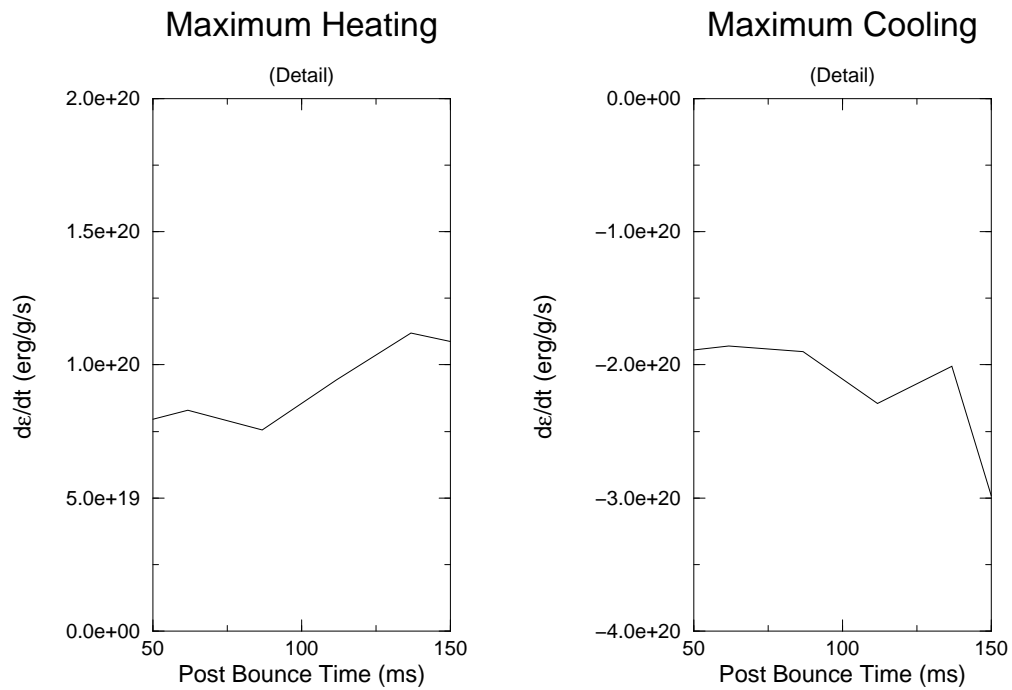


Fig. 10c.— Plots of the maximum net neutrino heating and net neutrino cooling rates as a function of time during the critical 50–150 ms after bounce.

Gain and Shock Radii vs. Post Bounce Time

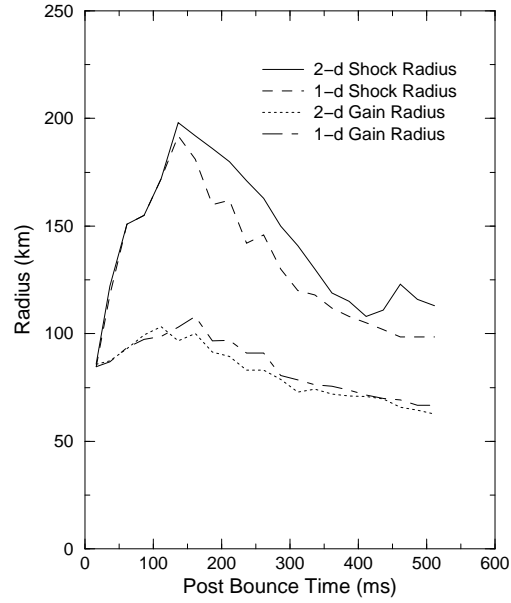


Fig. 11.— Plots of the angle-averaged gain and shock radii vs. time for our two-dimensional PPM simulation. Also shown for comparison are the gain and shock radii from our 1D PPM simulation.

Mass in the Gain Region vs. Time

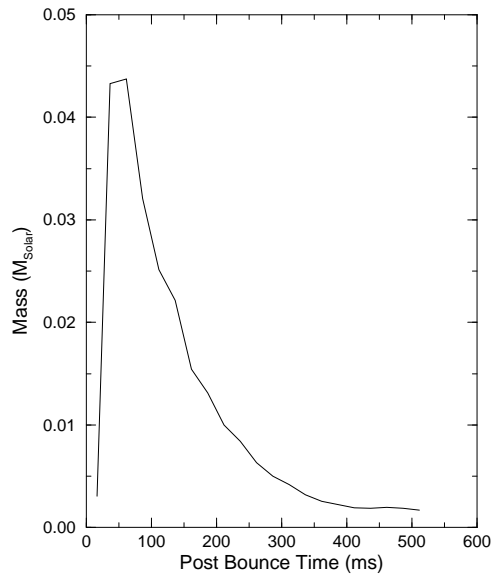


Fig. 12a.— Plot of gain region mass vs. time for our two-dimensional PPM simulation.

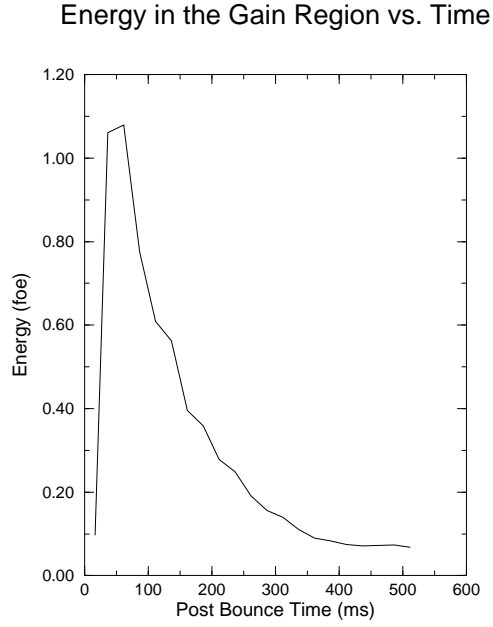


Fig. 12b.— Plot of gain region internal energy vs. time for our two-dimensional PPM simulation.

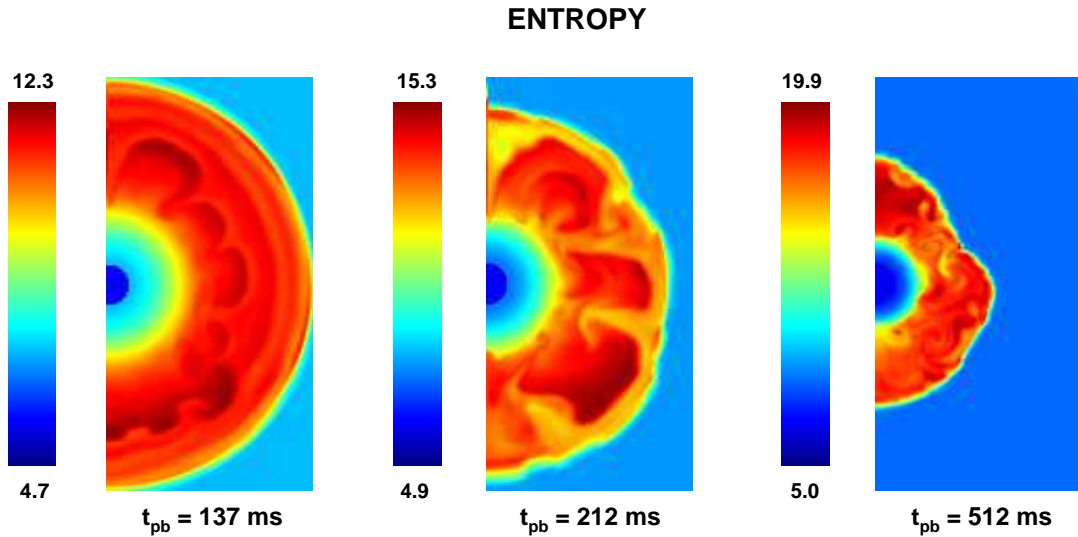


Fig. 3a.— Two-dimensional entropy plots showing the evolution of neutrino-driven convection in our $15 M_{\odot}$ model, at 137, 212, and 512 ms after bounce.

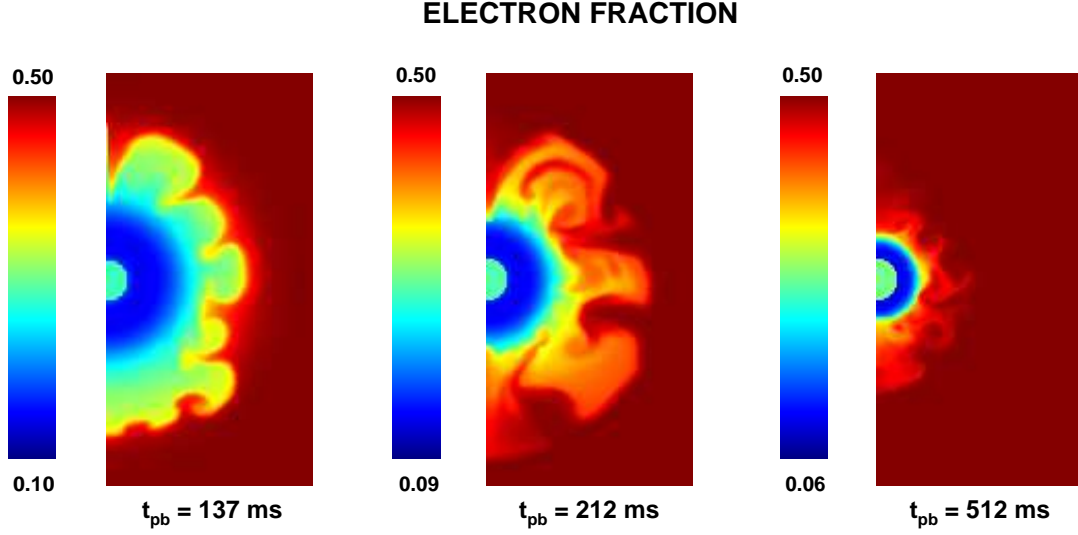


Fig. 4a.— Two-dimensional electron fraction plots showing the evolution of neutrino-driven convection in our $15 M_{\odot}$ model, at 137, 212, and 512 ms after bounce.

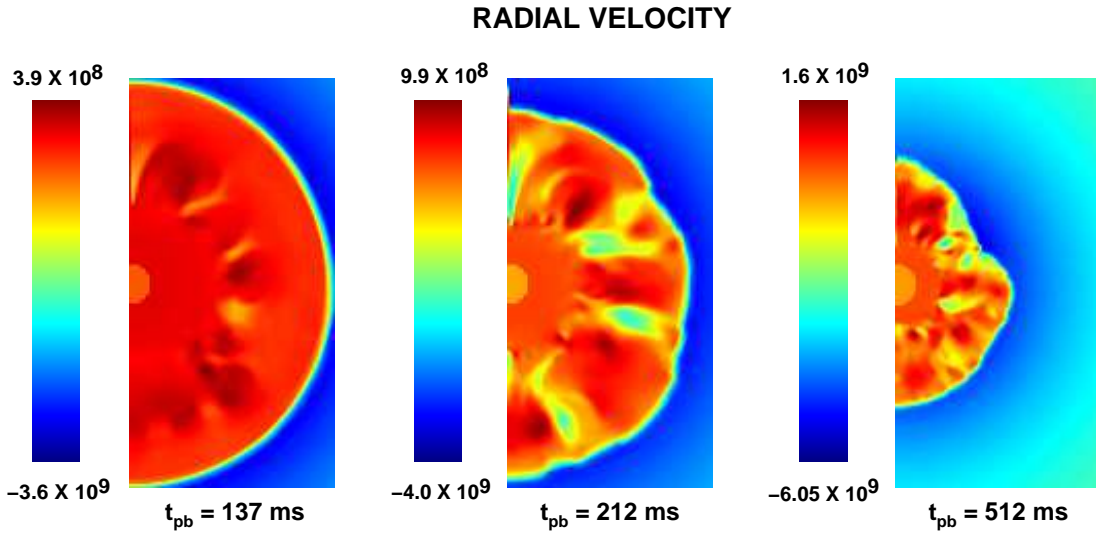


Fig. 5a.— Two-dimensional radial velocity plots showing the evolution of neutrino-driven convection in our $15 M_{\odot}$ model, at 137, 212, and 512 ms after bounce.

Comparison of 1D and 2D T and Y_e at $t_{pb} = 212$ ms

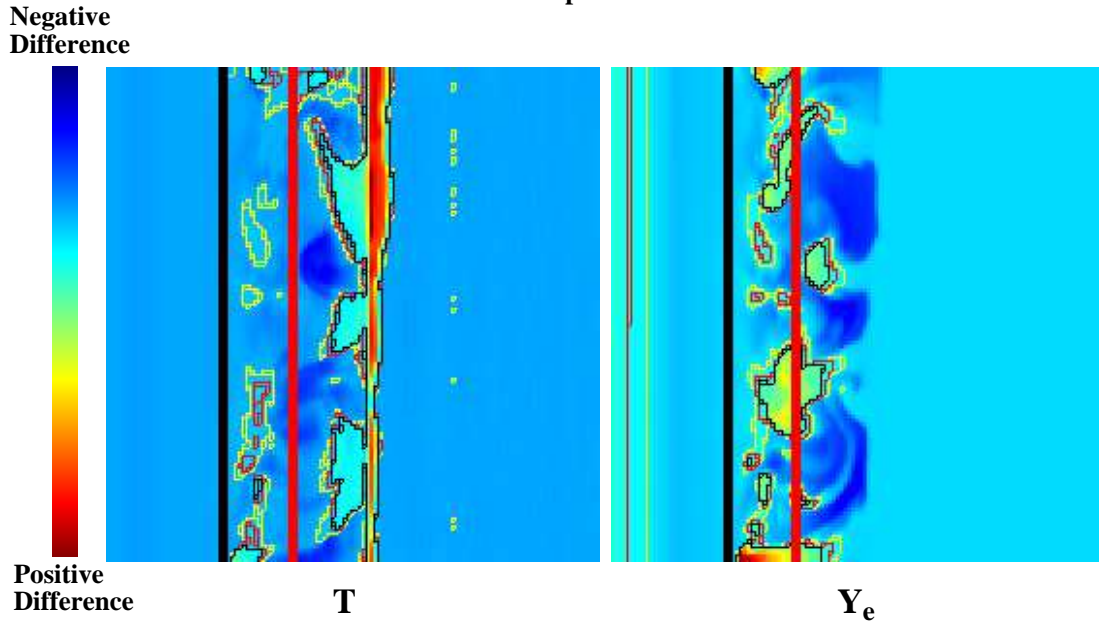


Fig. 13.— Plots showing the fractional differences between our one- and two-dimensional PPM simulations. Shown are differences in temperature and electron fraction. The panels are a Cartesian mapping of our two-dimensional grid, with 128 angles along the y -axis and 128 radii along the x -axis. The contours mark fractional differences of 3% (yellow), 6% (red), and 9% (black). The thick vertical lines mark the angle-averaged neutrinosphere and gain radii, in black and red, respectively.